

University of Alberta

**Fabrication and Characterization of Organic and Inorganic Linear
Nanostructures**

by

Joel Boulet

A thesis submitted to the Faculty of Graduate Studies and Research
in partial fulfillment of the requirements for the degree of

Master of Science

in

Microsystems and Nanodevices

Electrical and Computer Engineering

©Joel Boulet

Spring 2013

Edmonton, Alberta

Permission is hereby granted to the University of Alberta Libraries to reproduce single copies of this thesis and to lend or sell such copies for private, scholarly or scientific research purposes only. Where the thesis is converted to, or otherwise made available in digital form, the University of Alberta will advise potential users of the thesis of these terms.

The author reserves all other publication and other rights in association with the copyright in the thesis and, except as herein before provided, neither the thesis nor any substantial portion thereof may be printed or otherwise reproduced in any material form whatsoever without the author's prior written permission.

For Barb

She makes the world a better place

Abstract

Research was undertaken into the organic semiconductors tris(8-hydroxyquinoline)aluminum (Alq_3) as well as bis(8-hydroxyquinoline)zinc (Znq_2) to the effect of improving achievable morphological control using an inexpensive evaporation-based solution synthesis method. By varying experimental parameters such as ambient temperature, vapour pressure, choice of anti-solvent used and exposure time, growth and nucleation were optimized so as to produce organic single crystals. Two methods were discovered to grow arrays of vertically-aligned Alq_3 nano/micro rods out of a thin film of Alq_3 . Afterward, dielectrophoresis (DEP) was studied as a means to align linear nanostructures onto testing pads for characterization. To that effect, a DEP alignment platform containing seventy-four testing devices was designed and then constructed using microfabrication techniques such as electron beam evaporation and photolithography. Alignment of individual nanowires have been successful, and electrical measurements have been performed on p-type copper oxide yielding a hole mobility of $25.5 \text{ cm}^2/\text{Vs}$.

Acknowledgements

Firstly I would like to thank my supervisor Dr. Karthik Shankar for his financial support and for his continuous stream of ideas and suggestions over the course of my degree. His commitment to research is unparalleled in this galaxy.

I would also like to thank the members of my thesis committee, Dr. Doug Barlage and Dr. Eric Rivard for taking the time out their jam-packed schedules and teaching/research commitments to read my scratchings on the wall in the insane asylum and help me graduate. I appreciate it.

I'd like to thank my colleagues Arash Mohammadpour and Samira Farsinezhad for their contributions towards this thesis. They fabricated the inorganic nanorods and nanotubes used in the dielectrophoresis experiments. I also think they secretly developed time dilation technology which allows them to work for forty-plus hours every day. Very wisely they are keeping it to themselves so they appear to be superheroes to the rest of the world.

My thanks also go to the Nanofab and its staff. Every time I enter it I feel like a kid in a candy store, where each piece of candy is worth millions of dollars and the kids are all wearing shoe covers. In particular, I'd like to thank Mr. Les Schowalter. No one else can make a four hour training session on e-beam evaporation fun and engaging without resorting to beer or fireworks.

I would also like to be able to thank Dr. Randy Kobes from the University of Winnipeg. Dr. Kobes taught an advanced fourth-year electromagnetics course in the summer of 2010 just for me, so I could graduate without having to take general relativity. He was always willing to go the extra mile for his students, and we loved him for it (and for his beard he'd always tug whenever he was thinking). Unfortunately I had already completed my undergraduate honours thesis when he did this favour for me, so I told him I'd thank him in my Master's thesis. Dr. Kobes died of lung cancer two months later.

Last but not least I'd like to thank my best friend and wingman Andy Coleman. In addition to providing graphical figures for my thesis and my published scientific papers, Andy can always be counted on to take my mind off my woes and brighten any day. He is one of the few people I know who can equal me in a debate or in a game, and I love him for it. His character is of the highest standard, evidenced by his good-natured tolerance of my abrasive and egomaniacal behaviour even when I swoop in and use Dagon's at the last possible moment. I hope I can continue to prove worthy of his friendship.

Table of Contents

CHAPTER 1: INTRODUCTION

1.1: Introduction to Inorganic Nanostructures.....	1
1.2: Introduction to Organic Nanostructures.....	7
1.3: Thesis Statement.....	12

CHAPTER 2: LITTERATURE REVIEW

2.1: Nucleation Theory.....	13
2.2: Dielectrophoresis Theory.....	17
2.3: Anodization/Annealing Method.....	21
2.4: Solution Evaporation Method.....	24

CHAPTER 3: EXPERIMENTAL RESULTS AND ANALYSIS

3.1: Design and Fabrication of a Dielectrophoresis Platform.....	27
3.2: Electrical Measurements.....	38
3.3: Organic Growth Patterns.....	40

CHAPTER 4: CONCLUSION

4.1: Conclusion and Future Work.....	51
--------------------------------------	----

BIBLIOGRAPHY.....	54
-------------------	----

List of Tables

Table 1: Summary of the quantities and types of devices present on the DEP platform.....32

List of Figures

Figure 1: Computerized graphical representation of a single-walled carbon nanotube.....	2
Figure 2: Electron-hole separation in a vertical nanorod-based solar cell.....	4
Figure 3: The seven Bravais lattice types.....	5
Figure 4: Stacked organic molecules with and without an offset.....	10
Figure 5: Flexible OLED on display.....	11
Figure 6: Gibbs Free Energy diagram.....	15
Figure 7: The almost-linear dependence of nucleation rate on saturation energy.....	17
Figure 8: The dielectrophoretic force caused by a non-uniform electric field.....	19
Figure 9: Formation of a two-dimensional latex crystal, displayed as a function of time.....	20
Figure 10: Copper hydroxide nanowires formed via anodization.....	23
Figure 11: Roadmap detailing the various paths nucleation and growth can take.....	25
Figure 12: Interdigitated electrode fingers used for DEP alignment.....	28
Figure 13: Point-to-point square pads used for DEP alignment.....	29
Figure 14: The final photomask design used for fabricating DEP platforms.....	31
Figure 15: Close view of the target areas for nanowire alignment.....	32
Figure 16: Sequential view of the DEP platform fabrication process.....	37

Figure 17: Aligned nanowires for both an overpowered and correctly calibrated system...	38
Figure 18: Current-voltage measurements of a copper oxide nanowire.....	39
Figure 19: Final apparatus used for solution evaporation crystallization.....	42
Figure 20: The effects of temperature on Alq3 crystallization.....	44
Figure 21: The effects of temperature on Znq2 crystallization.....	45
Figure 22: The effects of pressure on Alq3 crystallization.....	46
Figure 23: The effects of pressure on Znq2 morphology.....	47
Figure 24: The effects of exposure time on crystalline rods.....	48
Figure 25: Vertical Alq3 microrod growth.....	49
Figure 26: Dense, oblique Alq3 microrod growth.....	50
Figure 27: Alq3 photoluminescence data.....	51

List of Abbreviations

AC: Alternating Current

ALD: Atomic Layer Deposition

Alq₃: tris(8-hydroxyquinoline)aluminum

DC: Direct Current

DEP: Dielectrophoresis / Dielectrophoretic

EBE: Electron Beam Evaporation

FET: Field Effect Transistor

HMDS: Hexamethyl disilazane

LED: Light-Emitting Diode

MTBE: Methyl tert-butyl ether

OLED: Organic Light-Emitting Diode

PL: Photoluminescence

SCLC: Space-charge limited current

SEM: Scanning Electron Microscope

VLS: Vapour-Liquid-Solid

XRD: X-Ray Diffraction

Znq₂: bis(8-hydroxyquinoline)zinc

Chapter 1: Introduction

1.1: Introduction to Inorganic Nanostructures

In the late twentieth century, personal computers revolutionized the world. For the first time, humanity reached greater heights by striving to build smaller rather than larger. The miniaturization trend continues to this day, as tablets and smartphones push aside laptops and phone booths. It is thus imperative for scientists and engineers to have a solid understanding of the nano- and micro-sized materials which are essential to the next generation of devices produced via nanotechnology[1]. Today, nanotechnology is a rapidly-expanding field which contributes directly to advanced structural materials[2-4], sensors[5-7], field-effect transistors (FETs)[8-10], and photovoltaics[11-13] as well as many other areas of research.

Linear nanostructures frequently form the metaphorical and literal building blocks of micro- and nano-scale devices. Typically cylindrical in shape (though hexagonal and rectangular prisms are also common), they are referred to as nanorods or nanowires when solid, and as nanotubes when hollow See Figure 1. The fundamental yet simple nature of the linear shape makes it an important component in most device designs.

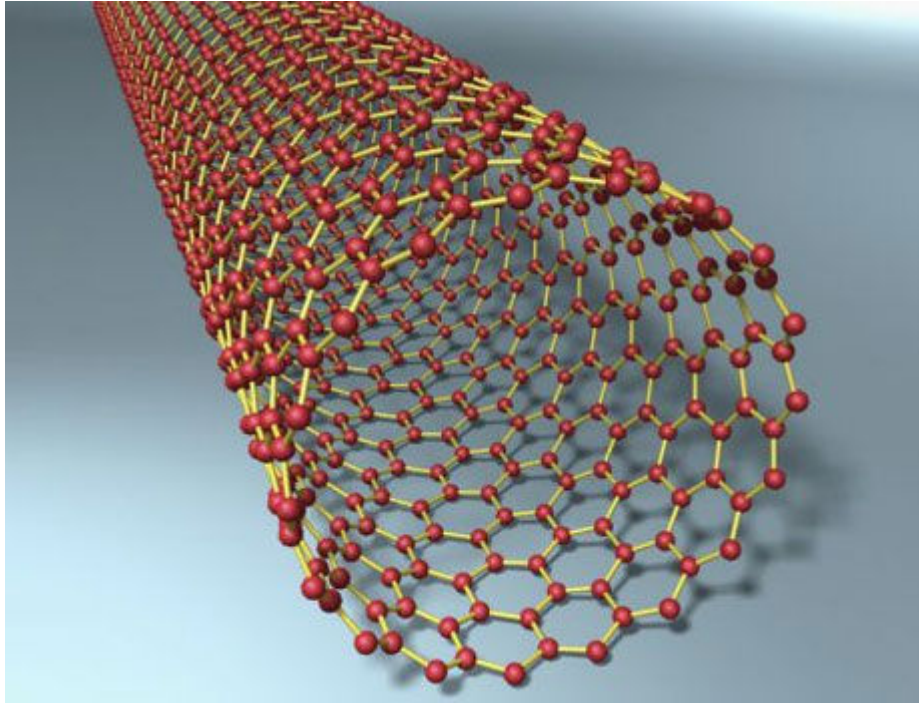


Figure 1: Computerized graphical representation of a single-walled carbon nanotube[14]

FETs, for example, require a semiconducting channel between the source and drain electrodes which will conduct either a large or small amount of electrical current (the 'on' and 'off' states for the transistor, respectively). This basic design requirement can be readily accommodated via nanotube or nanorod. A third terminal, known as the gate, has a voltage applied to it which generates an electric field inside the channel region. Depending on the channel material, the applied electric field can either increase the number of available charge carriers or decrease it, resulting in high or low conductivity in the channel, and thus the 'on' and 'off' states. In 1998, a FET was fabricated using one single-walled carbon nanotube[15]. With a length of only 100nm, the whole channel could be described as a single molecule – an important step forward in the ongoing efforts to miniaturize electronics.

As another example, photovoltaics can make excellent use of linear nanostructures. In a typical planar-type pn-junction solar cell, there is a fundamental compromise which must be made between wanting a thick semiconductor layer to maximize photon absorption, and wanting a thin semiconductor layer to minimize recombination as the electron-hole pair travels to the junction. An array of vertical nanorods offers a promising way to overcome this problem, as the two aforementioned priorities are orthogonalized so that they may coexist. With a vertical semiconducting nanorod engulfed by a semiconductor of the opposite type, the full length of it may be used to maximize photon absorbance while simultaneously its narrow radius allows for a short travel distance between the electron-hole pair creation and the pn-junction, minimizing recombination. See Figure 2 for a graphical representation of the three-dimensional nature of this design. In 2009, Fan et. al. demonstrated a proof of concept using this design, with the successful creation of a CdS/CdTe solar cell with 6% efficiency after little in the way of optimization[16]. Using vertical nanorods, the solar cell proved more efficient than a planar design with comparable CdTe thickness, which reported an efficiency of 5% [17].

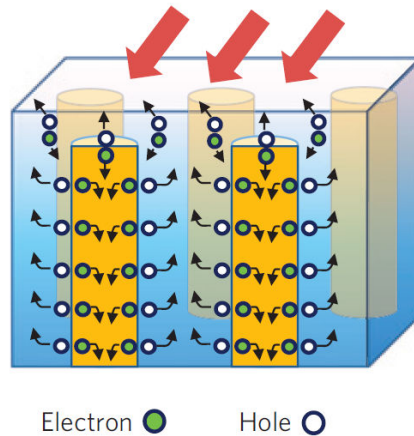


Figure 2: Electron-hole separation in vertical nanorod-based solar cell. Reprinted by permission from Macmillan Publishers Ltd: [Nature Materials] [16], copyright 2009.

A key variable in the determination of the quality of a material is its crystallinity. Crystallinity is a measure of a material's internal order, namely how well the particles conform to a periodic mathematical lattice of points[18]. There are seven types of periodic lattices which are used to describe the periodicity of crystalline materials, as shown in Figure 3. An object is considered to be single crystalline if its entire structure fits a single crystal lattice, with a certain tolerance for defects. A polycrystalline object is defined as containing pockets of single crystallinity which are separated by grain boundaries[19]. The bonds spanning across grain boundaries are longer and less consistent than those within a single crystal. Additionally, the crystal pockets do not typically share the same crystal orientation with each other, even if their lattice types are identical. An object is classified as amorphous if it lacks the internal long-range order to be considered crystalline or polycrystalline.

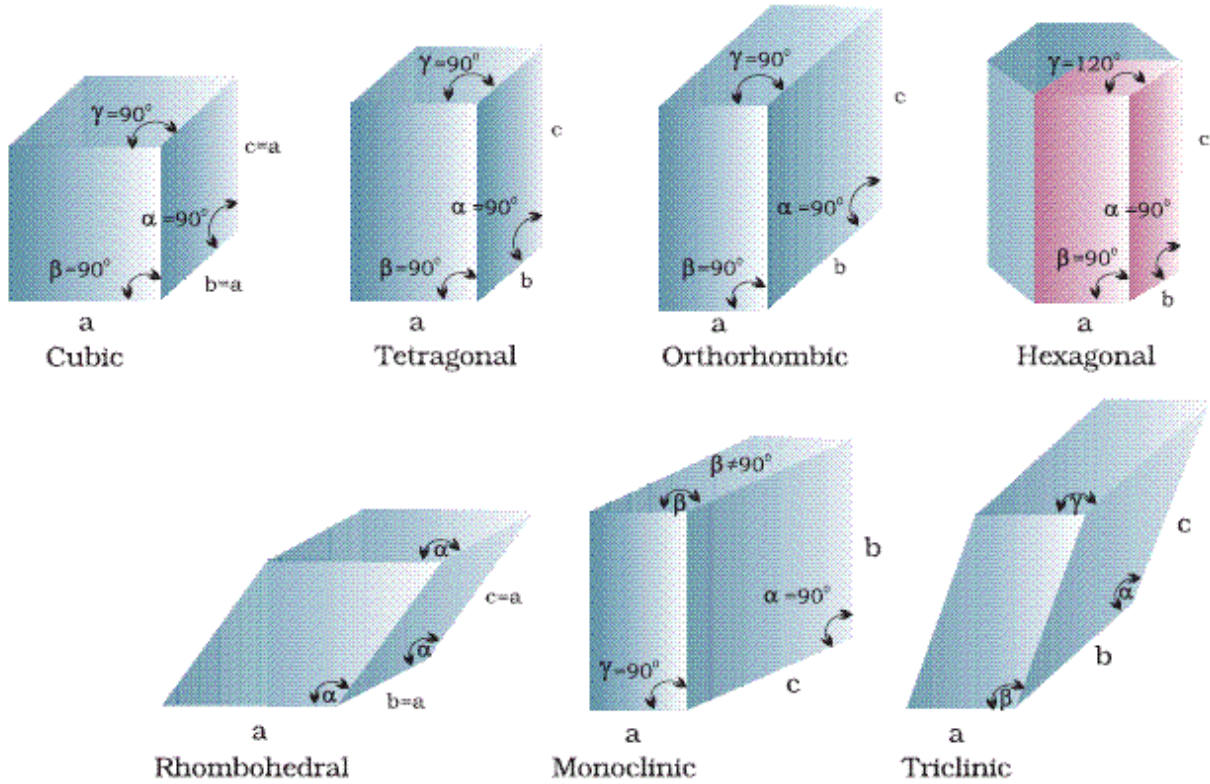


Figure 3: Seven Bravais lattice types[20]

The presence of defects is a near-certainty in any given crystal. A crystal defect can either be positional or compositional[21]. A compositional defect refers to the presence of an atom or molecule which is foreign to the crystal. The foreign contaminant may occupy a position in the lattice if its size and electrical properties resemble the atom or molecule which should be present for an ideal crystal. In semiconductor applications, this type of defect is frequently inflicted on a semiconductor in a controlled manner (doping) so as to increase or decrease the number of charge carriers present in the material[22]. Alternatively, a foreign contaminant may exist inside the lattice without joining it, by residing in the spaces inbetween atoms or molecules.

Positional defects refer to a disruption in the location of points within the lattice. A positional defect can be zero-dimensional, such as the absence of an atom or molecule from the lattice, leaving a void. A one-dimensional defect refers to a line of non-ideal bonding, such as could be found on an improperly-formed carbon nanotube, for example. A two-dimensional defect represents a plane of non-ideal bonds, such as a grain boundary in a polycrystalline material. A three-dimensional defect refers to a volumetric distortion of the crystal lattice, such as those formed by pores or large cracks[23].

Crystalline purity confers many advantages on the material in question, particularly with regards to optical and electronic properties. In atomic materials with low crystallinity, the typical bond length between atoms increases[21]. This has the effect of increasing the quantum mechanical potential energy barrier between atoms, restricting the transfer of electrons from one atom to another with the net effect of lowering the material's charge carrier mobility – one of the most important electronic properties for any material. Gaps in the crystal lattice or abrupt lattice termination at an outer surface can create dangling bonds. These are partially unbound atoms which act as zero-dimensional quantum wells (traps) for charge carriers. Traps decrease carrier mobility as well as carrier concentration[24].

Optically, undesired defects in the semiconductor's crystal lattice can manifest as irregular absorption and transmission of photons. A semiconductor's bandgap refers to the energy difference between its most energetic valence state and its least energetic conduction state[25]. When atoms are in close proximity to each other, the quantum mechanical states allowed for its charge carriers begin to split apart as the Pauli Exclusion

Principle forbids the existence of two fermions in the same state. The splitting of the energy states also typically increases the bandgap as a function of atomic or molecular proximity[26]. Conversely, when the bond length between atoms or molecules increases (as is usually the case when positional crystalline defects are present), this effect is reversed and the bandgap decreases until such time that the energy levels are no longer splitting due to lattice point proximity. Both solar cells as well as quantum well-based light-emitting diodes (LEDs) benefit from calibrated bandgaps within its semiconductors for maximum photon absorption and emission efficiency[27, 28]. In solar cells, bandgap shortening caused by crystalline defects decreases the useful energy absorbed per photon[29], whereas in LEDs this manifests as a divergence in the colour produced[28].

1.2: Introduction to Organic Nanostructures

The fundamental difference between organic and inorganic semiconductors is in their fundamental organizational divergence, as inorganics are formed from lattices of atoms whereas organics are formed from lattices of molecules. Organic semiconductors almost always have longer bonds comprising their lattices compared to inorganics due to the inter-molecular van der Waal forces being much weaker than the inter-atomic covalent bonds. The resultant fundamental property differences between these types of materials originate from this. The increased distance between molecules manifests as a lower electronic mobility for the organic material, due to the augmented quantum mechanical potential energy barrier each electron or hole must surpass in order to jump between molecules. Within an individual molecule, the dominant sigma bonds ensure low inter-

atomic spacing, however the overall ease of carrier passage within the overall material is determined by the worst segment of the path taken by an electron or hole, such that the efficiency of carrier travel across short intra-molecular bonds is dwarfed by the difficulties of traversing long inter-molecular bonds which act as bottlenecks to electric current.

The size of a molecule in comparison to the size of an atom also renders doping far more difficult for organic semiconductor operations. For standard inorganic semiconductors, doping is a process whereby atoms foreign to the crystalline composition of the target semiconductor are injected into the target material so as to displace its atoms in favour of the dopant. These impurities take the form of either donor (electron-giving) or acceptor (hole-giving) atoms so as to increase the number of electrons or holes present in the material. For modern applications, doping is essential to fabricating devices as it allows for a base material such as silicon or gallium arsenide to be custom-tailored for the relevant application. The size discrepancy between an atom and a molecule renders conventional doping impossible in organic semiconductors as the dopant atoms cannot properly fit into the molecular lattice.

There are two types of doping possible for molecular semiconductors: substitutional and interstitial, both of which have been demonstrated experimentally albeit in a limited number of cases. Interstitial doping refers to the insertion of atoms or molecules within the molecular lattice without joining the lattice. The dopant exists as a free atom or molecule loosely confined by the lattice molecules. This type of doping has been shown to increase the conductivity of organic semiconductors by six orders of magnitude[30]. However, due to the fluid nature of the dopant within the lattice, the conductivity and carrier

concentration of the material can vary wildly depending on ambient conditions. The instability of this type of material results in a short useful lifespan, and the unpredictability of the electrical properties precludes it from commercial device applications for the time being.

The other type of molecular doping demonstrated thus far is substitutional doping, whereby a new dopant molecule replaces the previous precursor molecule in the lattice itself. This type of doping is very difficult to achieve due to added complexity, as the dopant molecule must not only be comparable to the precursor in terms of size but must also match the correct orientation relative to the lattice in order to bond properly. In addition, both the dopant molecule as well as the precursor material must possess a high degree of electron delocalization in order for the dopant molecule to contribute to the overall material. Thus far this method has only been successfully performed for a small number of case studies, however when successful it has augmented an organic semiconductor's conductivity by magnitudes comparable to interstitial doping[31] without the latter's inherent stability problems.

While molecular doping is rarely performed due to its many inherent difficulties, organic semiconductors can still be altered to change their properties, albeit to a far lesser degree. The molecular structure of the semiconductor can be chemically changed by adding or removing pieces such as carbon chains, functional groups, etc, so as to change the overall semiconductor's properties. For example, a molecule could be tailored to maximize pi-pi stacking so as to decrease inter-molecular bond length and increase mobility. See Figure 4. The van der Waal attractive forces will bring stacked molecules in perfect order on top of

one another, however this is often disrupted by Coulombic repulsion between charged areas of the molecule, resulting in an offset [32]. Depending on the direction and magnitude of the offset, the overlap between the pi orbitals will usually decrease though it will sometimes increase. This results in either a suppressed electronic bandwidth or occasionally an augmented one[33]. This process is also used to facilitate substitutional molecular doping, as minor functional group changes can increase or decrease the number of free carriers in a molecule while maintaining the original molecule's overall size and thermal properties. This makes such a modified molecule an ideal candidate for molecular substitutional doping as its near-identical composition relative to the precursor maximizes its chances for acceptance into the lattice[31].

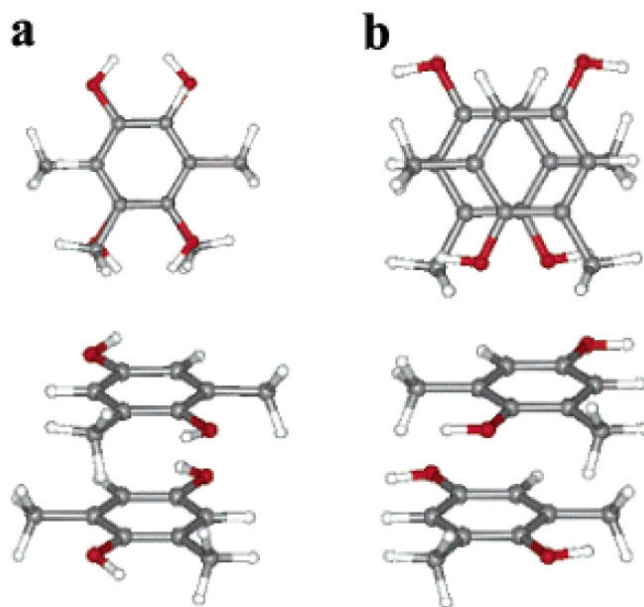


Figure 4: Two stacked 2,6-dimethylbenzene-1,4-diol molecules whereby a) is perfectly stacked and b) has an offset [34]. Reprinted (adapted) with permission from (Kim, K.S., et al., *Assembling Phenomena of Calix[4]hydroquinone Nanotube Bundles by One-Dimensional Short Hydrogen Bonding and Displaced π - π Stacking*. *Journal of the American Chemical Society*, 2002. 124(47): p. 14268-14279. Copyright (2002) American Chemical Society

The long inter-molecular bond length also creates unique advantages. Using a classical analogy, we can imagine an atomic or molecular lattice as a framework of springs.

Weaker bonds result in greater distances, but they also result in lower spring constants, which makes the overall lattice softer. Macroscopically, this manifests as a softer material, which is one of the primary advantages organic semiconductors have over inorganics as it allows for a flexible device, provided that the remaining device components can also be constructed with flexible materials (which is typically the case). So far, organics have been successfully used to make flexible active electronic displays[35-37], sensors[38-40], and transistors[41-43]. Figure 5 shows a flexible Organic Light-Emitting Diode (OLED).

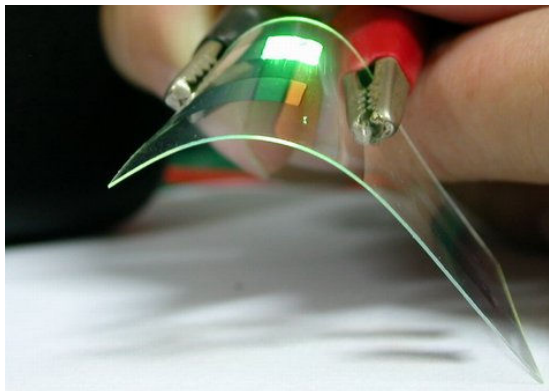


Figure 5: Present-day OLED being displayed functioning while bent[44]

In device applications, organic linear nanostructures are used in the same roles as inorganics, however the choice to use organics indicates a desire to utilize one or more of their unique advantages, typically flexibility or low-cost production requirements. Common production methods for inorganic nanostructures include

1. Vapour-Liquid-Solid (VLS)[45], which requires very high operating temperatures ($\sim 1000^{\circ}\text{C}$) as well as specialized equipment to control gas flow rate
2. Solvothermal[46], which requires very high internal pressure as well as a strong air-tight chamber to withstand the process

3. Template (electrophoretic)[47], which requires a porous membrane, a variable electric field, and a material which is ionic in solution.

By contrast, the common production methods for organic nanostructures tend to be simpler and less expensive to prepare:

1. Casting[48], which requires only a substrate and solvent suitable for the material
2. Physical Vapour Deposition[49] which requires a furnace and gas flow apparatus
3. Surfactant-Assisted Evaporation[50] which requires a surfactant, centrifuge, and hotplate.

1.3: Thesis Statement

The objective of this thesis is to fabricate and then characterize a variety of organic and inorganic linear semiconducting nanostructures. Organic nanostructures do not have as much established literature describing essential properties such as morphological control and electrical behaviour as their inorganic counterparts. As it is a rapidly expanding field of study, it is vital to establish this solid scientific foundation so as to allow for greater technological end products. Inorganic semiconductors have been extensively studied for decades, and yet in spite of this there remain unexplored avenues of research specifically in the domain of characterizing individual linear nanostructures of high purity. The undertaking of research into such a wide variety of topics including chemistry, physics, electrical engineering, and materials engineering will create a larger breadth of knowledge gleaned for the author at the conclusion of this degree.

Chapter 2: Literature Review

2.1: Nucleation Theory

The study of nucleation and growth is important to the field of solution-processed organic semiconductors. Nucleation is the process whereby a distinct thermodynamic phase of atoms or molecules forms out of a medium[51]. This can take the form of either homogeneous nucleation, whereby the nucleus is released from a uniform medium, or it can take the form of heterogeneous nucleation, whereby the nucleus is released on the surface of a material which is distinct from the medium.

A critical component to creating conditions whereby nucleation can take place is supersaturation[52]. Supersaturation is defined as the potential energy difference between an atom/molecule in solution versus one in crystal phase. Mathematically, this is shown[53] as

$$\Delta\mu = \mu_s - \mu_c = kT * \ln \left(\frac{c}{c^*} \right)$$

where

- $\Delta\mu$ is the supersaturation energy
- μ_s is the chemical potential energy of the particle in solution
- μ_c is the chemical potential energy of the particle in crystal phase
- k is the Boltzmann constant
- T is the absolute temperature
- c is the solution concentration

- c^* is the equilibrium saturation
- S is the supersaturation ratio $\frac{c}{c^*}$.

If the supersaturation energy is positive, then the solution is said to be supersaturated and nucleation becomes thermodynamically viable. Otherwise, the solution is undersaturated and dissolution takes place, which is the opposite of nucleation.

While being in a state of supersaturation allows for nucleation, it does not guarantee that nucleation will take place nor does it yield the nucleation rate. To determine this, we must examine the contribution of both volumetric and surface effects. The Gibbs free energy (ΔG) is defined[52] as the sum of volumetric free energy (ΔG_v) and surface free energy (ΔG_s). Assuming that a nucleated particle is spherical with radius r , then this can be expressed as

$$\begin{aligned}\Delta G &= \Delta G_s + \Delta G_v \\ &= 4\pi r^2 \gamma + \frac{4}{3} \pi r^3 G_v\end{aligned}$$

where

- γ is the interfacial tension between the developing crystalline surface and the supersaturated solution
- G_v is the free energy change of the transformation per unit volume.

The volumetric term represents the present bonds between lattice points, which can be interpreted as an existing energy debt. The surface term represents the end of the lattice, and thus the lack of an existing bond, which can be interpreted as positive energy relative

to lattice bonds. While γ is a positive value, G_v is negative and so the volumetric and surface terms compete with each other to determine whether the Gibbs free energy is positive or negative. Given that both of these terms are radially dependent, it should be possible to determine the critical radius (r^*) at which they cancel each other perfectly.

$$\frac{d}{dr}\Delta G = 8\pi r \gamma + 4\pi r^2 G_v = 0$$

$$r^* = \frac{-2\gamma}{G_v}$$

And so for $r < r^*$, a nucleated crystal will encounter a progressively stronger potential barrier compelling it back into solution as its radius increases, whereas for $r > r^*$ an increasing radius will stabilize it outside the solution. At the critical radius, $\Delta G(r)$ becomes $\Delta G(r^*) = \Delta G^*$ which is the maximum energy barrier preventing nucleation. We can see a visual representation of the Gibbs free energy as a function of radius in Figure 6.

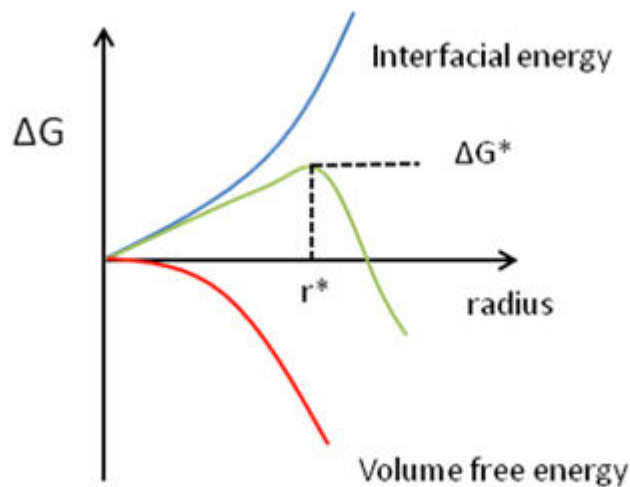


Figure 6: The Gibbs free energy as a function of radius, with volumetric and surface components decomposed[54]

The supersaturation energy ($\Delta\mu$) of a solution is related[53] to the volumetric Gibbs energy of the system as

$$\Delta G_v = -n\Delta\mu$$

$$\frac{4}{3} \pi r^3 G_v = -nkT * \ln(S)$$

$$\frac{-2\gamma}{r^*} = \frac{-nkT * \ln(S)}{\frac{4}{3} \pi r^3}$$

$$r^* = \frac{8\pi\gamma r^3}{3nkT * \ln(S)}$$

where n is the number of atoms/molecules forming the cluster. This equation demonstrates a relationship between the critical radius of nucleation and the degree of supersaturation present in solution. As supersaturation increases, so too does the critical radius decrease, allowing for easier nucleation. This inverse relationship has also been experimentally confirmed[55].

The quantitative difference between homogeneous and heterogeneous nucleation is the change in the interfacial tension γ [53]. The presence of a surface in heterogeneous nucleation offers energy in the form of dangling bonds (unbound valence electrons) which decreases the value of γ and thus also decreases the Gibbs free energy potential barrier, allowing for easier nucleation. This also manifests as a lowering of the critical supersaturation point.

The nucleation rate J_{nuc} can be determined[52] via Arrhenius-type equation

$$J_{nuc} = A e^{\frac{-\Delta G^*}{kT}}$$

whereby the prefactor A is also dependent on supersaturation. A plot of this as a function of supersaturation energy is provided in Figure 7, with the critical supersaturation marked.

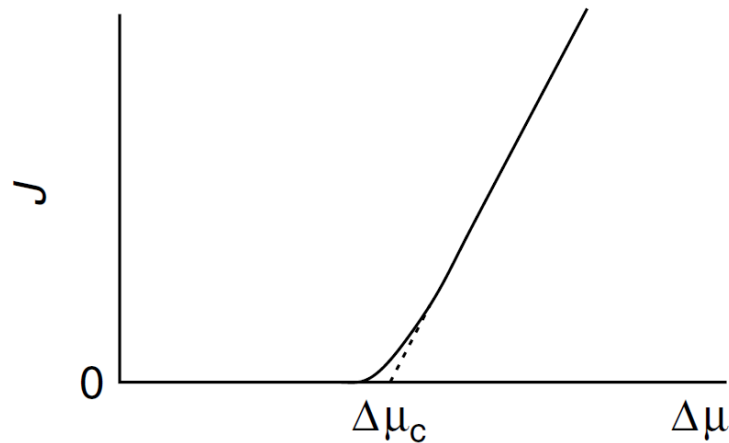


Figure 7: The almost-linear dependence of nucleation rate on supersaturation energy[53]

2.2: Dielectrophoresis Theory

Dielectrophoresis (DEP) is a term first coined by Pohl in 1978 as “the motion of suspensoid particles relative to that of the solvent resulting from polarization forces produced by an inhomogeneous electric field”[56]. DEP is a technique through which electrically neutral matter may be propelled solely through the use of electric fields. Upon first examination, this would seem to violate Coulomb’s Law

$$\vec{F}_e = q \vec{E}$$

due to the target object’s net charge being nil. This would seemingly make it impossible to generate a force regardless of the electric field being applied.

Suppose that the targeted object was a lossless dielectric material. Its charges would polarize the object in accordance with the direction of the ambient electric field. For a sphere, the dipole moment can be expressed [57] as

$$p = 4 \pi \varepsilon_m R^3 \frac{(\varepsilon_p - \varepsilon_m)}{(\varepsilon_p + 2 \varepsilon_m)} E$$

where

- p is the dipole moment
- ε_m is the absolute permittivity of the surrounding medium
- ε_p is the absolute permittivity of the targeted object
- R is the radius of the sphere
- E is the ambient electric field.

While polarized, the sphere may be thought of as two half-spheres, each of which carries a net electric charge which is equal and opposite to the other. The positive half-sphere would be compelled via Coulombic force to travel along the electric field lines, whereas the negative half-sphere would be compelled to travel against them. Since the net charge on each half is identical and the electric force acting on each half is identical, the two opposite forces cancel each other and the whole sphere undergoes no motion.

However, if the electric field is non-uniform, then the two halves of the sphere would experience different magnitudes of Coulombic force, and there would be a net movement. This is the fundamental principle of DEP [56]. The simplest way to create a non-uniform electric field is to generate a voltage between two asymmetrical electrodes, as demonstrated in Figure 8.

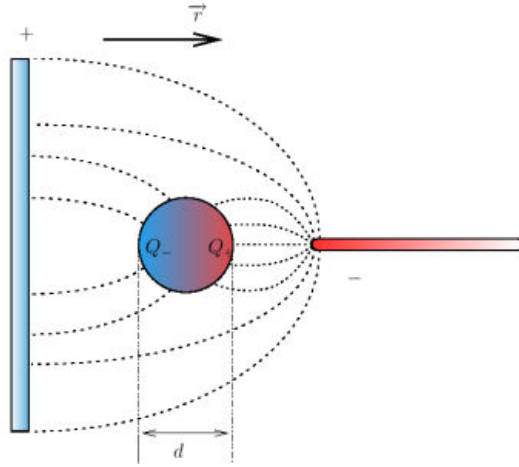


Figure 8: The dielectrophoretic force caused by a non-uniform electric field[58].

Starting with the above expression for the dipole moment, an equation describing the DEP force is found [57] to be

$$F_{DEP} = 2 \pi \varepsilon_m R^3 \frac{(\varepsilon_p - \varepsilon_m)}{(\varepsilon_p + 2 \varepsilon_m)} (\nabla E^2)$$

for a sphere. Note that $\nabla E^2 = 2E\nabla E$, which indicates that both the magnitude of the electric field as well as its rate of change where it intersects the particle are proportional to the DEP force.

Currently, there are many uses for DEP as a manipulation/filtration/assembly tool. While most micro-scale devices rely on a bulk layered approach to fabrication, the ability to assemble a device from pre-made discrete components (such as linear nanostructures) is immensely valuable as it makes those discrete components equally viable for device applications. Linear nanostructures can have superior electrical properties to their bulk counterparts, however those advantages are wasted if they cannot be integrated into practical devices. Specifically in the domain of carbon, DEP has been used to assemble organized bundles of nanotubes [59], separate semiconducting and conducting carbon

nanotubes from one another into homogenous groups [60] and attracting nanotubes onto patterned electrodes for transistor fabrication [61, 62]. Different types of sensors have also been fabricated using DEP, such as strain sensors [63] and humidity sensors [64]. With regards to gas sensors, it has proven instrumental in the construction of devices capable of detecting NH_3 [65], NO_2 [66, 67], CO [68] and H_2 [69]. It has also been used as a tool for characterizing semiconducting nanostructures, such as GaN [70-72] and ZnO [73, 74].

Most of the aforementioned applications involve using DEP as a way to manoeuvre a nanotube or nanorod onto a platform so as to complete a device, however it can also be used to form the applicable nanostructure itself. Arrays of gold nanorods have been formed using DEP and a porous alumina template [75], as have highly-ordered two-dimensional latex crystals from a suspension of microparticles in water [76], shown in Figure 9.

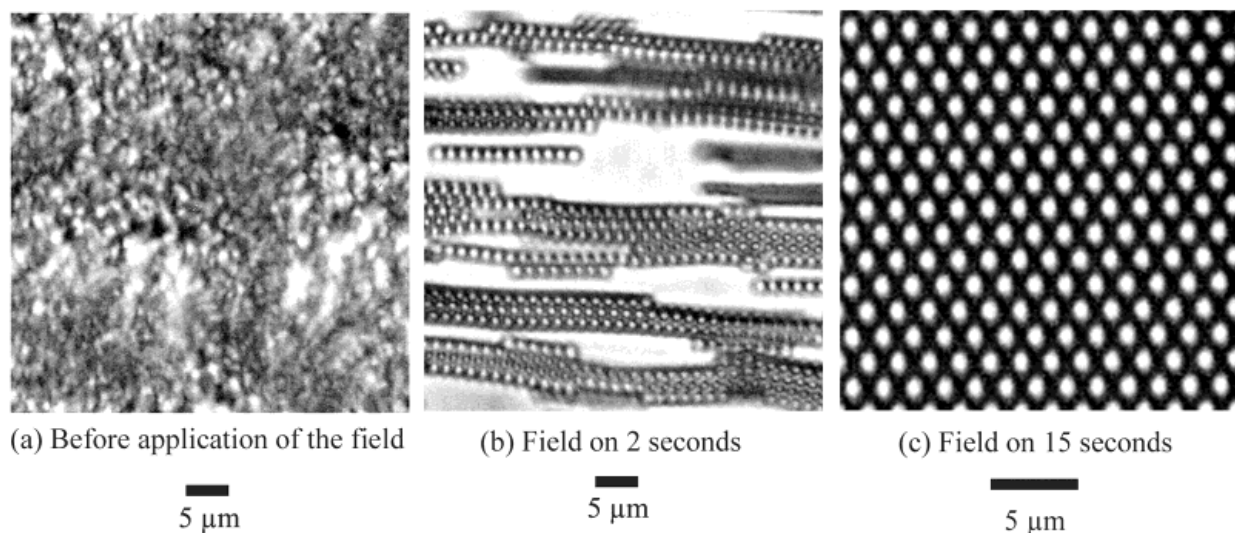


Figure 9: Formation of a two-dimensional latex crystal, displayed as a function of time [76]. Reprinted (adapted) with permission from Lumsdon, S.O., E.W. Kaler, and O.D. Velev, *Two-Dimensional Crystallization of Microspheres by a Coplanar AC Electric Field*. *Langmuir*, 2004. 20(6): p. 2108-2116. Copyright (2004) American Chemical Society

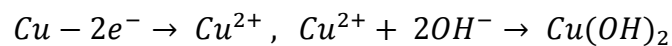
DEP's greatest contributions to science and technology so far have arguably been in the field of biological/medical research. As a filtration mechanism, it is capable of filtering

out leukemia cells from normal healthy red blood cells [77], filtering parasite-infested cells from healthy cells [78, 79], separating one type of leukocyte (white blood cell) from another[80], or even containing viruses [81-83]. The potential use of DEP in this field is massive due DEP's non-destructive nature compared to centrifugation or chemical treatment. Likewise, DEP is desirable due to its effectiveness on any target particle so long as its size and dielectric constant do not result in an equal force exerted on both the target and a non-desired material also present in a sample.

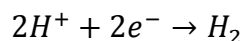
2.3: Anodization/Annealing Method

One of the key materials studied in this research is copper oxide (CuO). Bulk CuO possesses a bandgap of 1.35 eV [84] and has a deep black colour. These two factors make it a desirable material for solar cells, as the bandgap yields an efficient balance between energy gained per photon versus number of photons absorbed, and the black colour indicates a high degree of photon absorption.

The method used to grow copper oxide nanowires for this research is one of anodization to form Cu(OH)₂ nanowires followed by annealing into CuO nanowires. Anodization is a process whereby the target substrate (anode) is immersed in an electrolytic solution along with another substrate (cathode) whereby current passing between them creates two electrochemical half-reactions[85]. In the case of copper hydroxide[86] immersed in a 2mol/L aqueous KOH solution, these are



at the anode, and



at the cathode.

The mechanism for the formation of linear nanostructures is speculated by Zhang et al.[87] to be as follows. The growth process takes place in a non-equilibrium reaction system in which the different growth speeds of the crystal faces determine the ultimate morphology. The orthorhombic $\text{Cu}(\text{OH})_2$ consists of isolated chains in the planes (001) which are oriented along (100) and characterized by the square planar coordination of the Cu^{2+} ions with strong $\sigma_{x^2-y^2}$ bonds. The Cu^{2+} ions form another two longer and more ionic bonds with two OH^- groups from neighbouring chains along the c-axis, completing a deformed octahedron in the first coordination sphere of Cu^{2+} . By juxtaposing the chains this way, one obtains a corrugated sheet parallel to (010). A three-dimensional $\text{Cu}(\text{OH})_2$ crystal is formed by stacking of these sheets through hydrogen bonds.

The experimental parameters are noteworthy. If the KOH concentration is too low (<0.5M) for example, then there are insufficient hydroxide ions present and the $\text{Cu}(\text{OH})_2$ does not form[86], turning the experiment into the simple hydrolysis of water. If the concentration is too high (>3.5M) then the abundance of hydroxide ions causes dehydration in the $\text{Cu}(\text{OH})_2$, reducing it to bulk CuO. While CuO is the desired final product, the CuO formed in this manner is that of a thin film as it does not grow preferentially in the (100) direction from the copper foil's lattice as $\text{Cu}(\text{OH})_2$ does. The $\text{Cu}(\text{OH})_2$ thus serves as an intermediary to establish the desired morphology. See Figure 10 for SEM images of the $\text{Cu}(\text{OH})_2$ nanowires grown in this fashion. X-Ray Diffraction (XRD) data taken from the

Cu(OH)₂ samples show that this method produces single crystals[86], whereas a purely wet chemical process can only produce polycrystalline Cu(OH)₂[88-90].

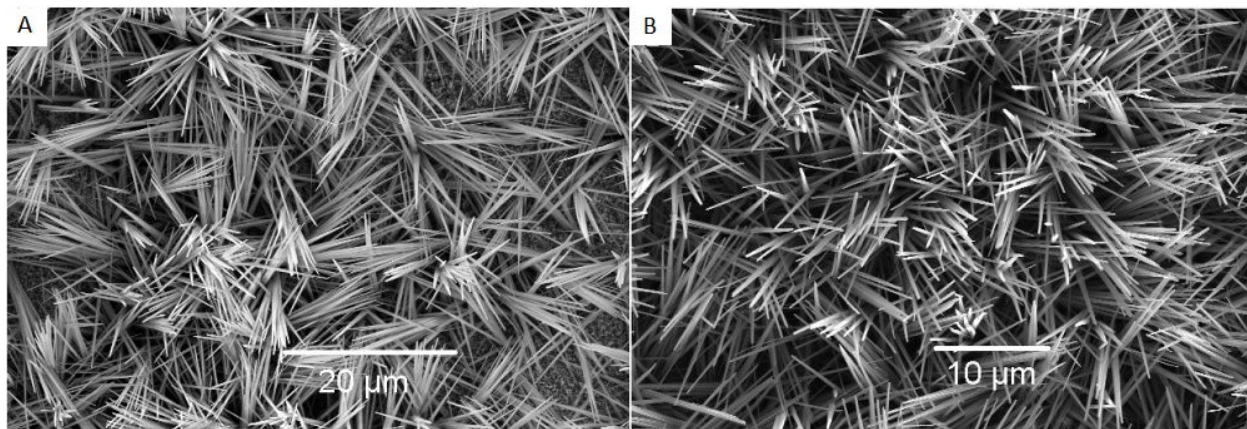
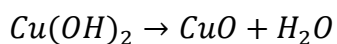


Figure 10: Copper hydroxide nanowires grown via anodization, with a) 1000s exposure time and b) 1500s exposure time[86]. Reprinted (adapted) with permission from Wu, X., et al., *Copper Hydroxide Nanoneedle and Nanotube Arrays Fabricated by Anodization of Copper*. *The Journal of Physical Chemistry B*, 2005. 109(48): p. 22836-22842. Copyright (2005) American Chemical Society.

After the anodization is complete, it becomes necessary to anneal the sample to convert it to CuO[91]. The Cu(OH)₂ nanowires on Cu foil are placed inside a tube furnace with the ambient air replaced by a steady stream of N₂. Over the course of twelve hours, the temperature rises to 180°C before being allowed to cool slowly. Over the course of the annealing, the Cu(OH)₂ is dehydrated such that



and the color clearly changes from blue to black. CuO produced in this manner was found to be single crystalline, based on XRD data taken[92]. Unfortunately this method also produces a quantity of Cu₂O amidst the CuO, which can bring to question the validity of experimental results for CuO.

2.5: Solution Evaporation Method

It is a common theme when studying organic semiconductors to begin with a bulk quantity of the material which is then dissolved in solution only to then be driven out of the solution in a particular manner so as to achieve a desired thin film or crystalline nanostructure. Solution processability is very desirable due to its simple and inexpensive requirements[37]. Most commonly, a thin film is formed by simple evaporation in air[93-96] however this often results in an amorphous film or at best a polycrystalline one. Alternatively, single crystals can be grown in solution however this often relies on surfactants creating a micelle around a nucleus so as to limit growth to one dimension[50, 97, 98]. The use of surfactants is undesirable due to the surfactant's persisting and contaminating presence once the nanorods have been formed.

A solution-based approach to organic self-assembling crystal growth without use of surfactants is possible using an evaporation strategy[99, 100]. Figure 11 is an interesting roadmap detailing the possible avenues the crystallization process may undertake depending on the experimental parameters[101]. The crystal material begins at point A inside solution to a solvent which evaporates over time. As the solvent evaporates, the concentration increases until the solution becomes saturated at point B. At point C, the supersaturation is sufficiently high to begin nucleation of the crystal material. If the nucleation rate is high, then the solution quickly loses concentration faster than the evaporation decreases solvent volume and growth is slow from C to E. This results in a large quantity of small crystals. If the nucleation rate is moderate, then the solvent evaporation rate is matched by the nucleation rate, and the net concentration remains steady until there is no more material left in solution. In this case, the path taken is C' to F.

If the nucleation rate is low, then the solvent evaporates sufficiently more rapidly than nucleation such that agglomeration occurs, resulting in a small number of crystals growing rapidly. The path in that case is C'' to G. If the material in solution cannot crystallize, then the path taken is C to D, and the material will simply be a disordered residue once the solvent has completely evaporated.

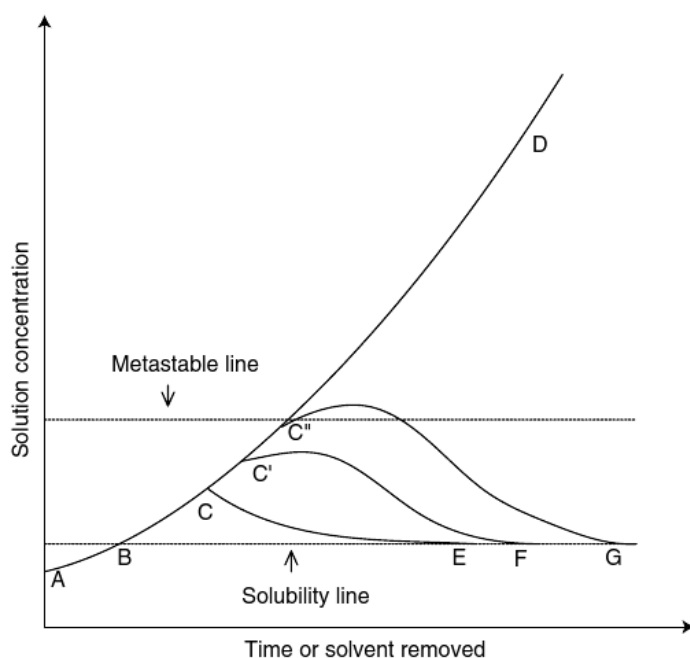


Figure 11: The possible courses taken by a crystallizing material in an evaporating solution-based self-assembly[101]

However, the evaporation method relies upon achieving a slow rate of growth during crystallization for high quality results. A slower rate of growth promotes superior crystallinity by granting time to new molecules to bond to its ideal position on an existing nucleus rather than being forced into a non-ideal bond. Planar pi-conjugated molecules, for example, will naturally self-assemble into ordered stacked rows[102, 103] given adequate environmental conditions. The absence of a large number of competing molecules (which are inherent to fast crystal growth) also means that any molecule which bonds to a nucleus

in a non-ideal location stands a chance of re-entering solution as its comparatively weak bond to the crystal can be broken, allowing the molecule to be recycled prior to a second attempt at perfect stacking. In this manner, single crystals can be grown.

There are currently two established methods used to achieve slow crystal growth in a solution-based process without use of surfactants. The first method is through the use of an anti-solvent[99, 104]. An anti-solvent is an agent which reduces the solubility of a material in a given solvent when added to the system. If a solution meets the supersaturation requirement for nucleation, then the addition of an anti-solvent increases the supersaturation ratio (S), which decreases the critical radius (r^*) and increases the nucleation rate. If the nucleation rate is augmented, then a larger number of seed crystals will be formed which will lower the quantity of remaining molecules (especially in close proximity to the newly-released crystal) in suspension and thus decrease crystal growth rate, as there are fewer candidates for growth still available.

The second method employed to decrease crystal growth rate in a solution process is to decrease the evaporation rate of the solvent. While some solvents such as water are fairly stable in standard atmosphere, most evaporate much more quickly due to having comparatively weaker inter-molecular bonds. The solvent evaporation rate can be slowed by containing the solvent within a positive-pressure vapour environment, as the solvent molecules are bombarded from all directions by gas particles which prevent their normal release into vapour. This has the effect of artificially keeping the solvent volume high, which decreases the concentration of semiconductor molecules in suspension and thus increases the average time until one such molecule impacts and bonds with a nucleus.

Chapter 3: Experimental Results and Analysis

3.1: Design and Fabrication of a Dielectrophoresis Platform

Due to the nature of the DEP force, namely that it is directly proportional to the gradient of the electric field, it is necessary for a DEP-based device to incorporate features of some sort so as to avoid creating a uniform electric field. The simplest way to accomplish this is with an asymmetric set of electrodes, such as those demonstrated in Figure 8. As we see there, particles would be attracted to the smaller of the two electrodes as it not only has a greater density of electric field lines, but those lines also demonstrate more curvature. This, while an effective design for a device which has the sole purpose of attracting dielectric matter, does not function well with regards to aligning that same matter. Assuming a two-electrode system, both electrodes need to be equally powerful in attraction to maximize chances that a nanotube or nanorod will come into contact with both and bridge the gap.

For the purpose of this thesis, it was desirable to not only attract and align linear nanostructures in suspension, but also to ensure that only one targeted object would be locked in place for study at any given time. Electrical diode and transistor measurements have been performed in the past on all materials studied in this research – in bulk form. However, as shown previously, crystallinity can differ greatly between a nanostructure and bulk material. It is therefore of scientific interest to study a single nanorod or nanotube at a time, and determine if its properties differ from the bulk. To that end, it was a design requirement to limit the area between electrodes such that there would be space for only one nanostructure at any given time.

One of the most commonly seen designs for DEP in the literature is that of the interdigitated electrode fingers, shown in Figure 12. The finger design[105] allows for high surface area between electrodes in a controlled manner. This can be very useful when seeking to align large quantities of nanowires at once. The upper field electrodes shown in Figure 12b serve as focusing lenses for the DEP force as it creates new electric field gradients at those points.

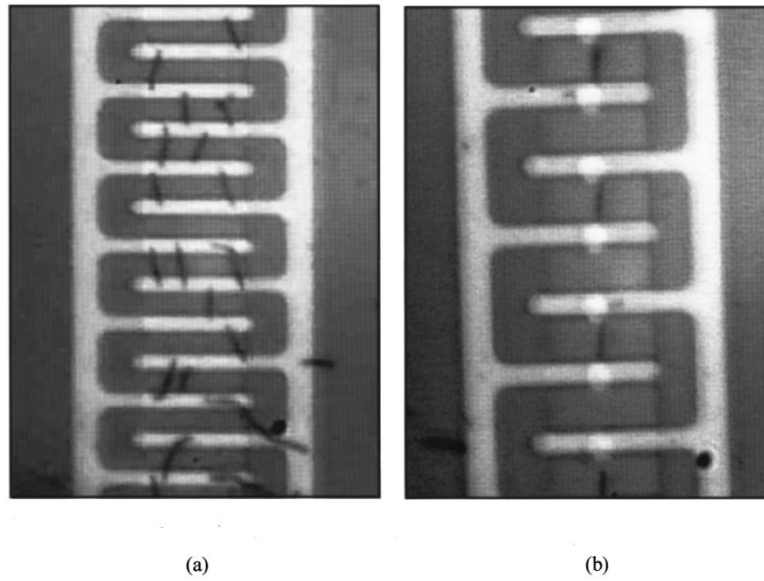


Figure 12: Interdigitated electrode fingers used for DEP, shown a) without upper field electrodes and b) with upper field electrodes[105]

Another design which is sometimes seen is that of the point-to-point square pads[106] as shown in Figure 13. Whereas the interdigitated fingers are designed to maximize surface area, the square pads are designed to do the exact opposite. By minimizing the area where the electrodes can be bridged by a nanowire, it decreases the probability that multiple nanowires will be inadvertently locked in place across the device.

However, this also decreases the probability of aligning anything at all. DEP is ultimately based on electric fields, which obey the inverse-square distance relationship. This places a great importance on the range of the target relative to the attractive DEP device. If a suspended nanowire is not directly above the one point where the square pads meet, it will not be drawn down to that target point and will thus fail to create a bridge across the electrodes.

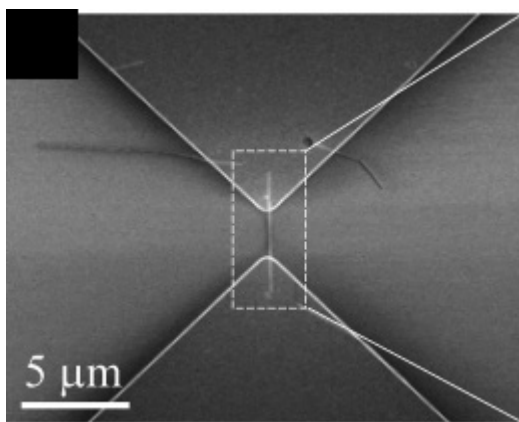


Figure 13: SEM image of point-to-point square pads used for DEP alignment[106]. Reprinted (adapted) with permission from Dong, L., et al., *Dielectrophoretically Controlled Fabrication of Single-Crystal Nickel Silicide Nanowire Interconnects*. *Nano Letters*, 2005. 5(10): p. 2112-2115.. Copyright (2005) American Chemical Society

Both design philosophies had merit, and so a mask for photolithography was designed such that both design types would be made in parallel. The interdigitated electrode finger design was sliced in pieces such that each electrode pair would have its own contact pads for probe measurement, as opposed to a single comb pad which contained many fingers. While this discretized approach is more costly in terms of surface area on a mask or wafer, it also is far more effective in taking electrical measurements for a single nanowire. Because the length of a nanotube or nanorod can vary from sample to

sample (and to make the device wafer relatively adaptable) both halves of the wafer feature size-varying iterations of the same design. Figure 14 shows the completed mask. Figure 15 demonstrates a close view of the two electrode archetypes. Table 1 presents a complete summary of all the devices present, in terms of their dimensional characteristics. Both design philosophies had macroscopically-sized contact pads for easy probe tip contact. Note that in Figure 14, the finger-design half of the mask appears to be a set of rectangles, when in fact each rectangle is a set of two electrodes with finger protuberances at their centres – the separation between the contact pads is too small to be seen without magnification.

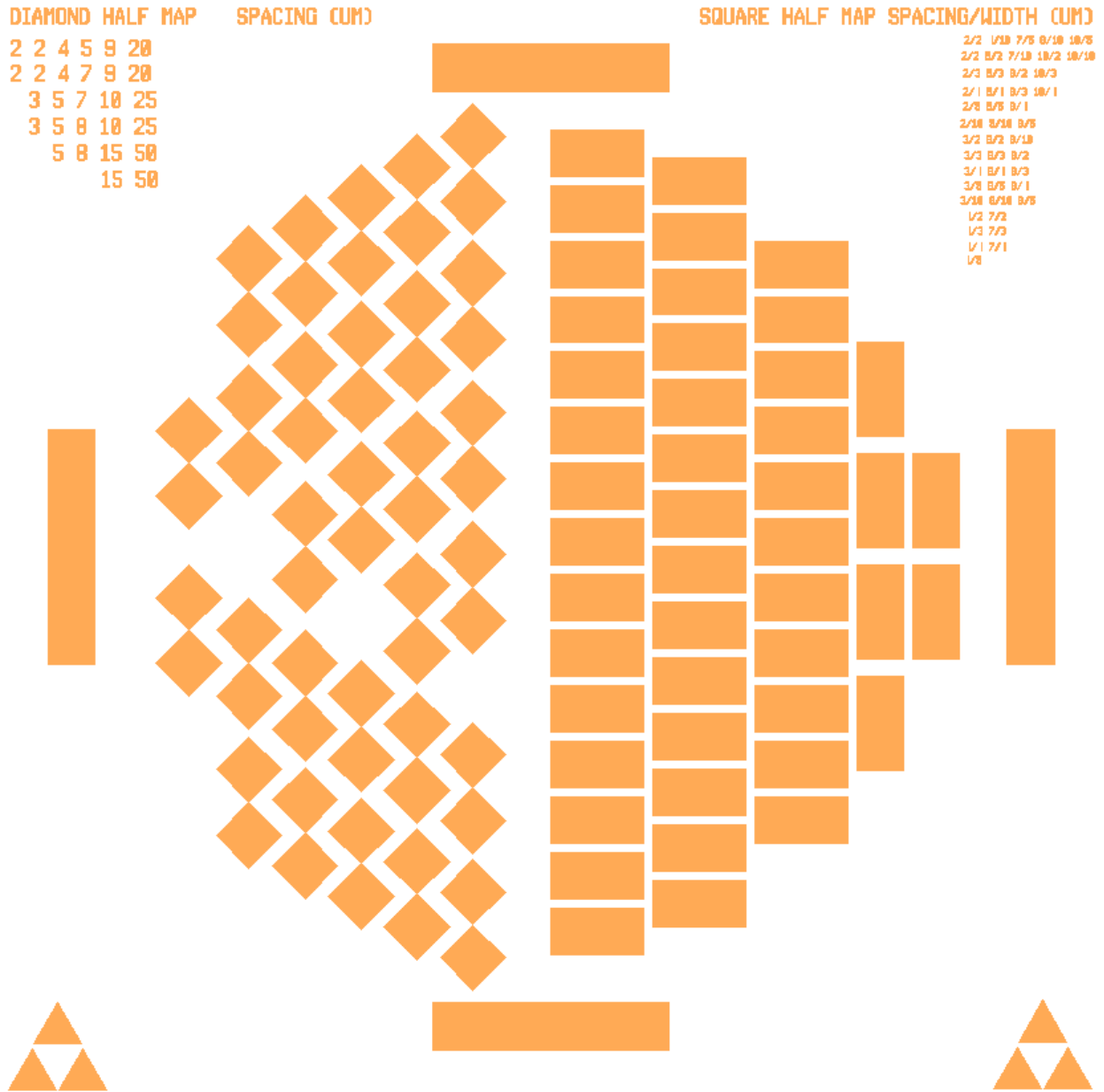


Figure 14: The photolithography mask designed for this thesis. The coloured regions represent the transparent zones on the otherwise chrome-finished mask.

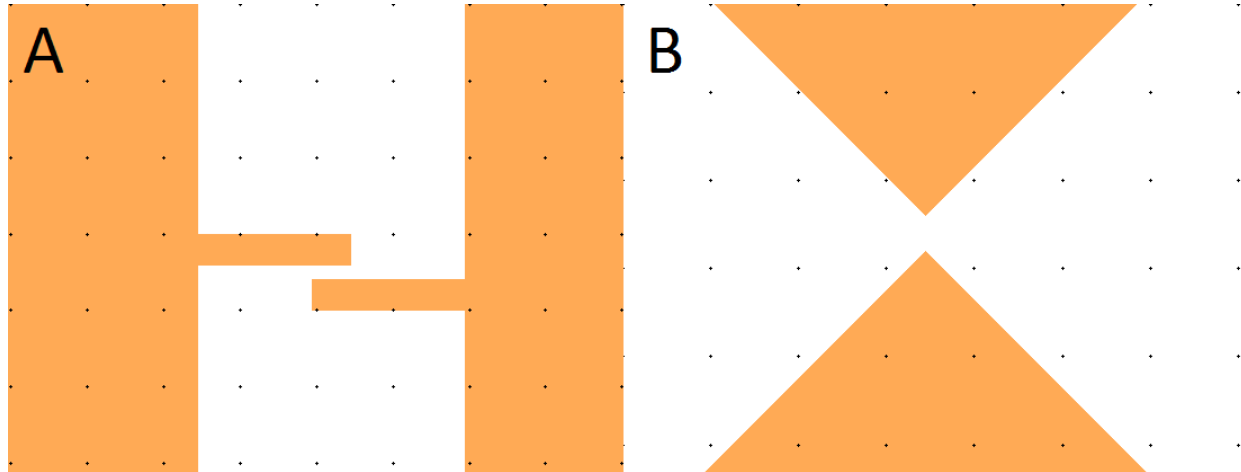


Figure 15: Close-in views of the areas to be bridged by an attracted linear nanostructure for a) the electrode finger design, and b) the point-to-point square pad design.

Electrode Spacing (um)	Width of Spacing (um)					
	N/A	2	3	4	5	10
2	4	2	1	1	1	1
3	2	1	1	1	1	1
4	2	1	1	1	1	1
5	4	1	1	1	1	1
6	0	1	1	1	1	1
7	2	1	1	1	1	1
8	2	1	1	1	1	1
9	2	1	1	1	1	1
10	2	1	1	1	1	1
15	2	0	0	0	0	0
20	2	0	0	0	0	0

25	2	0	0	0	0	0
50	2	0	0	0	0	0

Table 1: Number of devices of different types per device dimensions whereby green devices are of the square point-to-point architecture and the blue devices are of the electrode finger-type architecture.

The material composition of the DEP device is relatively straightforward. Silicon was chosen as a substrate due to its minimal roughness of $\pm 5\text{nm}$ [107], its ability to serve as a gate terminal for transistor measurements, and for its ease of use with virtually any nanoengineering process. Specifically, a silicon wafer with a single top layer of silicon dioxide was used since the SiO_2 serves as an insulator between any two electrodes and prevents current leakage. Gold was chosen as the bulk material for the electrodes due to its excellent conductive properties and its resistance to oxidation at room temperature.

Prior to the deposition of any materials, it is common to expose a fresh wafer to Hexamethyl disilazane (HMDS) vapour treatment. The silicon atoms (and accompanying methyl groups) in HMDS bond to the oxygen on the surface of the silicon wafer, creating a monomolecular silane layer. The resulting layer is slightly hydrophobic (which decreases water re-absorption after baking) and increases adhesion between the wafer and photoresist.

The patterned gold electrodes contain feature sizes as small as two microns, which is currently impossible to deposit directly to such great precision. It is therefore required to undergo an intermediary step known as photolithography to establish the desired feature pattern before a thin film of gold can be deposited. The process involves applying a thin layer (typically via spin-coating) of a photosensitive material known as photoresist which

is then baked into a solid thin film. An optical mask is then placed above the photoresist which obscures portions of the wafer from light as required by the desired features. Ultraviolet light is then targeted onto the wafer, and is allowed to strike the photoresist only where the mask is transparent. Depending on the type of photoresist, the exposed areas will either be strengthened or weakened by the radiation exposure. The whole wafer is then submerged in a developer, which is a specialized solvent fine-tuned to preferentially dissolve the weaker of the two photoresist areas. The final result is a layer of photoresist which remains on the wafer, which can be in any pattern desired within the minimum feature limits of the available equipment.

Two different methods were investigated as means to deposit the thin layer of gold once a patterned layer of photoresist was present on the wafer via photolithography. The first of these was sputtering, a mainstream technique whereby argon ions are accelerated towards a negatively charged target in a sealed vacuum chamber containing a bulk form of the desired metal to be deposited. Upon impact, the ions dislodge metal atoms which then bombard the substrate and form a thin film. Sputtering is a popular method because it operates at high deposition rates[108] (1-10nm/s) and can be used with a large variety of materials. Due to the energetic and turbulent nature of the particles in motion, the liberated atoms strike the target surface at non-trivial angles relative to the normal. This causes an enveloping effect whereby vertical surfaces not directly exposed to the source material are also coated with the thin film metal.

The second deposition method investigated was electron-beam evaporation (EBE).

EBE is a straightforward process whereby a bulk sample of the metal to be deposited is heated via electron beam, which frees metal vapour to rise in a vacuum-sealed chamber and nucleate on the target surface. EBE is not as popular as sputtering due to its slower deposition rate, typically 0.1-1.0 nm/s [108]. However, the slower nature of EBE can be an advantage, as the slowly-rising metal atoms do not collide strongly with each other and will thus settle on the target surface with angles near zero from the normal, meaning that only the top surface of the target wafer will be coated.

EBE was chosen to fabricate the DEP platform used in this research because, while being more time-consuming and expensive, it functions well for liftoff purposes whereas sputtering does not. Liftoff is a process whereby all remaining photoresist on a wafer is dissolved, and any deposited metal on top is separated from the rest of the wafer and simply floats away. Because sputtering also coats the side walls of a vertical feature, it forms a metal connection between the gold deposited on the wafer and the gold deposited on the photoresist atop the wafer. This defeats the purpose of liftoff, which requires a separation of the two layers of gold, such that after liftoff is complete the only remaining material on the wafer is the deposited gold in the desired pattern.

The entire sequence of steps used in the fabrication of the DEP platform will now be detailed in text as well as in Figure 16.

1. The N^+ Si/SiO₂ wafer is cleaned with piranha exposure lasting fifteen minutes. This removes all contaminants and ensures a smooth operating surface.

2. The cleaned wafer undergoes HMDS vapour treatment. First, the wafer is baked so as to remove all moisture. It is then exposed to a low pressure HMDS gas, which bonds to the surface of the wafer and releases ammonia.
3. The wafer is placed on a spin-coating chuck and locked in position via vacuum seal. A small quantity (5-10 mL) of the photoresist HPR 504 in liquid form is poured atop the wafer in the centre. The spin-coater activates at 500 RPM for ten seconds to evenly coat the whole wafer with photoresist before jumping to 4000 RPM for forty seconds so as to remove excess photoresist beyond a 1 micron thickness. The wafer with photoresist layer is then soft baked for 90 seconds at 115 °C. This solidifies the photoresist and gives it longevity for subsequent steps.
4. The photomask is locked in place above the photoresist layer, and is then exposed to UV radiation for 2.2 seconds. The wafer is then submerged in HPR 504 developer for twenty seconds to dissolve the unwanted, weakened photoresist and leaving only the desired pattern on the wafer.
5. A thin 10 nm layer of chrome is deposited onto the wafer and photoresist via EBE so as to serve as an adhesion layer between the silicon dioxide and the gold. Afterwards, 200nm of gold is deposited at a rate of 0.02 nm/s.
6. Liftoff is performed. The remaining photoresist is dissolved by immersing the wafer in an acetone bath inside an ultrasonicator for one hour.

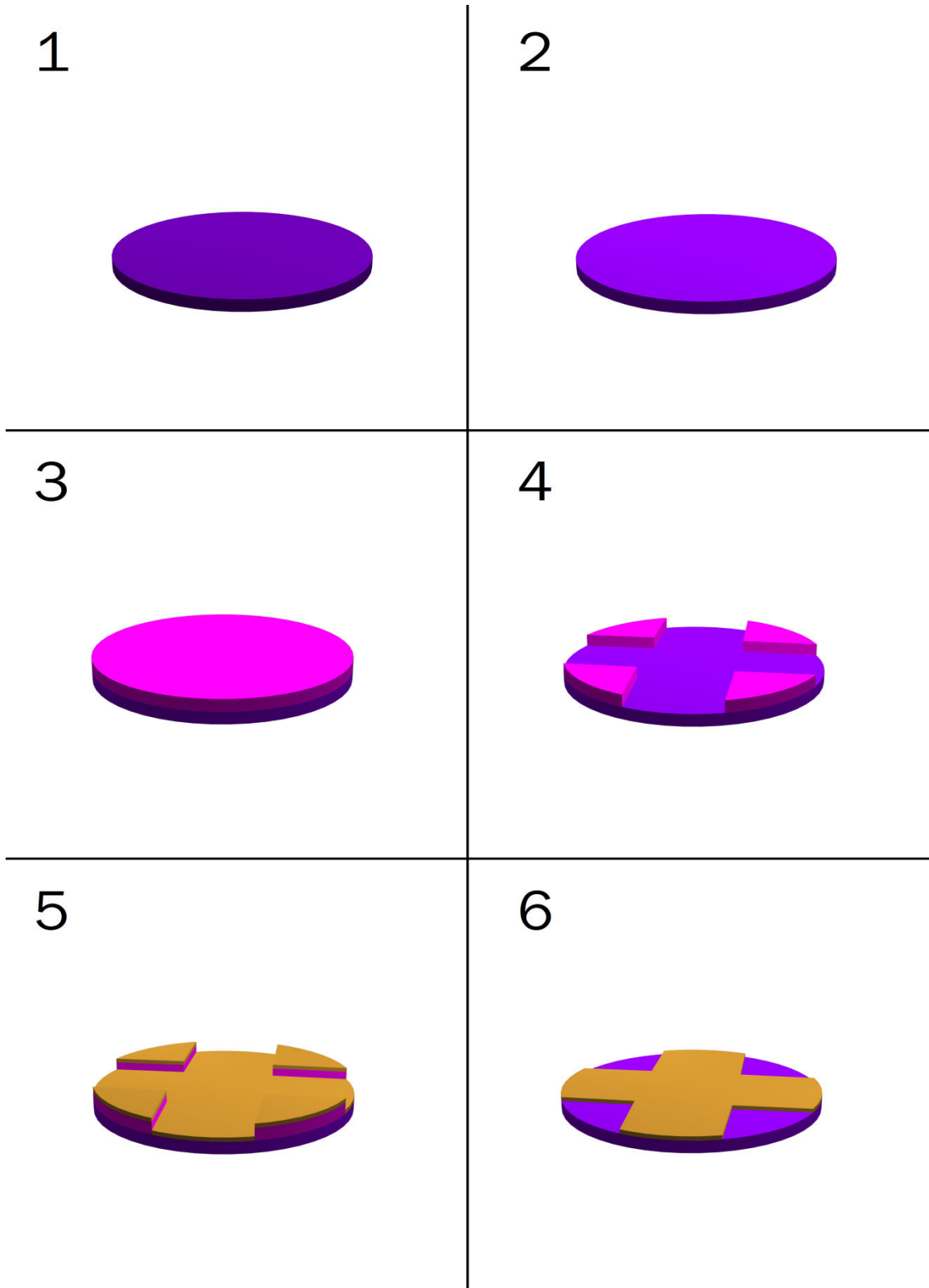


Figure 16: Illustration of the DEP platform process flow

3.2: Electrical Measurements

Using the DEP platform fabricated as described in the previous section, many inorganic nanowires were aligned across gold electrodes. The key parameters to be controlled were the choice of suspending liquid (ϵ_m), the applied voltage (V), as well as the concentration of nanowires in the suspending liquid. Depending on the experimental conditions, it was occasionally a balancing act between exerting too weak of a force (and thus failing to align anything) and exerting too strong of a force, which could either result in too many nanowires aligned or in the device being destroyed by heat. See Figure 17.

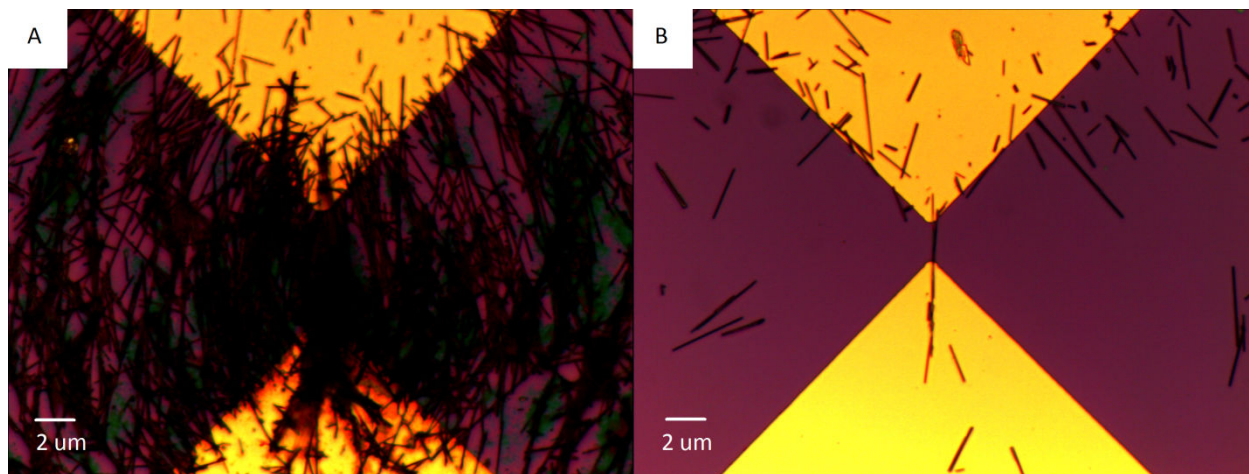


Figure 17: Examples of DEP alignment where a) the DEP force is too strong, and b) the DEP force is correctly calibrated

Once aligned, it was possible to subject the nanowires to diode (IV) measurements. Starting with a range of zero to fifty volts over a copper oxide nanowire of 250nm diameter and channel length of 7 μm , it was found to behave in a manner of ($I \propto V^2$) which is indicative[109] of space-charge limited current (SCLC), except perhaps for the low voltage region which appeared linear ($I \propto V$) and which is indicative of Ohmic resistance. A quadratic curve fit was applied to the I-V data, and found that it followed a quadratic curve with an adjusted R^2 value of 0.997. See Figure 18. When shifting to a log scale for both axes,

it becomes apparent that there are two distinct exponential regimes within the IV data, namely the Ohmic region from 0-6V (adj. $R^2 = 0.939$) and the SCLC region onward (adj. $R^2 = 0.992$).

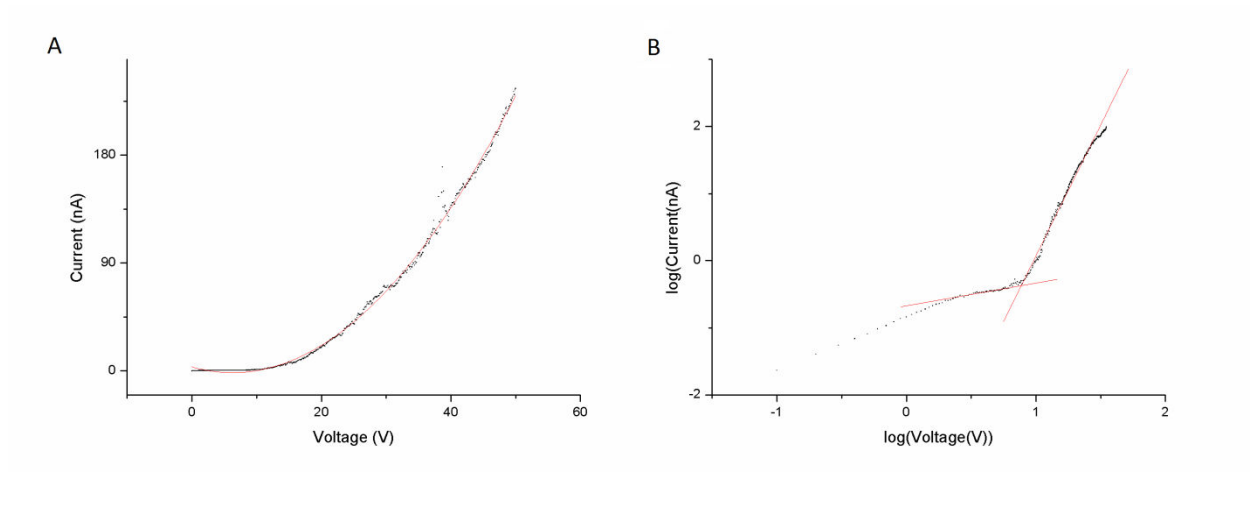


Figure 18: Diode measurements of a copper oxide nanowire with curve fitting on a) a regular scale, and b) a log scale

In an ideal trap-free system, the hole mobility of the aligned nanowire could be determined[110, 111] from the above data using the equation

$$J = \frac{9\varepsilon_r\varepsilon_0\mu_h V^2}{8L^3}$$

where

- J is the current density
- ε_r is the dielectric constant of the nanowire
- ε_0 is the permittivity of free space
- μ_h is the hole mobility
- V is the voltage
- L is the length of the nanowire across the channel.

However, in a real system containing traps, an additional multiplicative factor θ is required such that

$$\theta = \frac{N_c}{N_t} e^{\frac{-E}{kT}}$$

where

- N_c is the mobile carrier concentration
- N_t is the density of traps
- E is the trap depth
- k is the Boltzmann constant
- T is the temperature.

And so with the data currently available, it is possible to calculate an approximate hole mobility $\mu_h\theta$ of 25.5 cm²/Vs. This result is quite high for CuO, which suggests that there is a significant degree of Cu₂O contamination present from this fabrication process.

3.3: Organic Growth Patterns

Beginning with the approach demonstrated in the tris(8-hydroxyquinoline)aluminum (Alq₃) growth paper published by Xu et. al. [99], a great many crystal growth experiments via solution evaporation were performed over the course of a year, using both Alq₃ as well as bis(8-hydroxyquinoline)zinc (Znq₂). Initially the apparatus used was identical to that described in the paper, namely of a parafilm-sealed beaker containing a quartz substrate held above a moat of anti-solvent. The stock solution containing the Alq₃ is deposited atop the quartz, where it is surrounded by the vapours released by the anti-solvent moat. The holes in the parafilm allow the vapour to escape at a

significantly slower rate than would otherwise occur if the beaker were simply exposed to air. Because the anti-solvent moat is constantly evaporating, the internal environment is subjected to positive pressure which prevents outside air from entering the system and contaminating the anti-solvent vapour.

Over the course of experimentation, this apparatus evolved so as to be able to provide more reliable results. Firstly, the quartz substrate, while convenient for subsequent characterization due to its flat and transparent nature, did not contain the stock solution drop well as it had a tendency to slide off the edge. The quartz was replaced by a small plastic cup which had a shallow concave depression ideal for containing liquid. The cup was in turn later replaced by a flat titanium dioxide substrate deposited in an aluminum cavity. The TiO_2 substrate was flat and thus more useful for characterization work, and the aluminum well contained the stock solution drop and provided some shielding on the sides so as to limit convection in the anti-solvent vapour. The beaker and parafilm were also scrapped in favour of a glass jar with an airtight lid. Multiple lids were kept on hand, each with a hole of specific diameter drilled into the centre of it. These controlled-diameter lids were far more useful in regulating the experimental conditions of the crystallization, as parafilm holes were at best inconsistent in size, which in turn would dictate the internal pressure of the system. The final apparatus is shown in Figure 19.

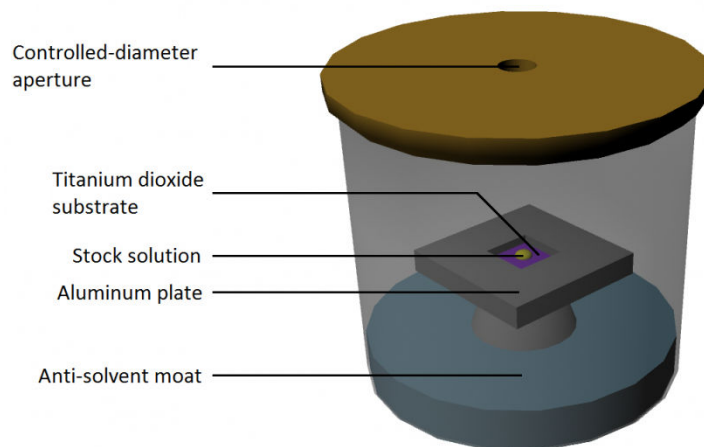


Figure 19: Final apparatus developed over the course of this research for evaporation-based crystallization

One of the key parameters investigated in this research which had not been explored in the literature was the effect of temperature on the solution evaporation process for crystallization. Obviously the temperature of the system will affect the inter-molecular spacing in the stock solution which in turn will vary the degree of supersaturation accordingly, however the temperature will also contribute to the level of volatility present in the anti-solvent vapour contained within the system.

Roughly three different temperatures were used over the course of experimentation, namely room temperature (20°C), refrigeration temperature (0°C), and freezer temperature (-25°C). Note that in all cases, THF was used as the stock solution unless indicated otherwise, with a typical volume being 20µL per sample. It was found to be universally true for all chosen anti-solvents that Alq₃ samples produced at 0°C had longer aspect ratios than those produced at 20°C. See Figure 20. The change in ambient temperature during crystallization caused an increase from approximately 3:1 aspect ratios to approximately 7:1. This can be attributed to a slower rate of growth inherent to a

lower temperature, as Alq₃ molecules were accorded more time to bond to preferential locations (the microrod tips) where pi-pi stacking results in a stronger bond. Additionally, crystals produced at lower temperatures displayed superior size and greater scarcity compared to those produced at room temperature. This is in perfect accord with the C' path described in Figure 11 as the lower temperature rendered nucleation more difficult versus the C path undertaken at room temperature. At freezer temperatures of approximately -30°C, however, different anti-solvents produced different results. Acetone and THF both produced short rods of dubious crystallinity, whereas diethyl ether and methyl tert-butyl ether (MTBE) were able to maintain their crystallinity as well as their aspect ratios. See Figure 20. This discrepancy can be explained by examining the relatively greater volatility of diethyl ether versus acetone or THF. As a measure of this, we observe that acetone and THF are accorded[112] an evaporation rate of 6.6 and 6.3 respectively versus butyl acetate whereas ether's evaporation rate is 11.8. Because gaseous volatility is decreased at a lower temperature, it is possible that the positive pressure environment induced by the anti-solvent vapour become too weak for acetone and THF once cooled to -25°C resulting in rapid solvent evaporation, whereas ether's naturally greater volatility granted it superior resistance and a continued impact on slowing the stock solution's evaporation.

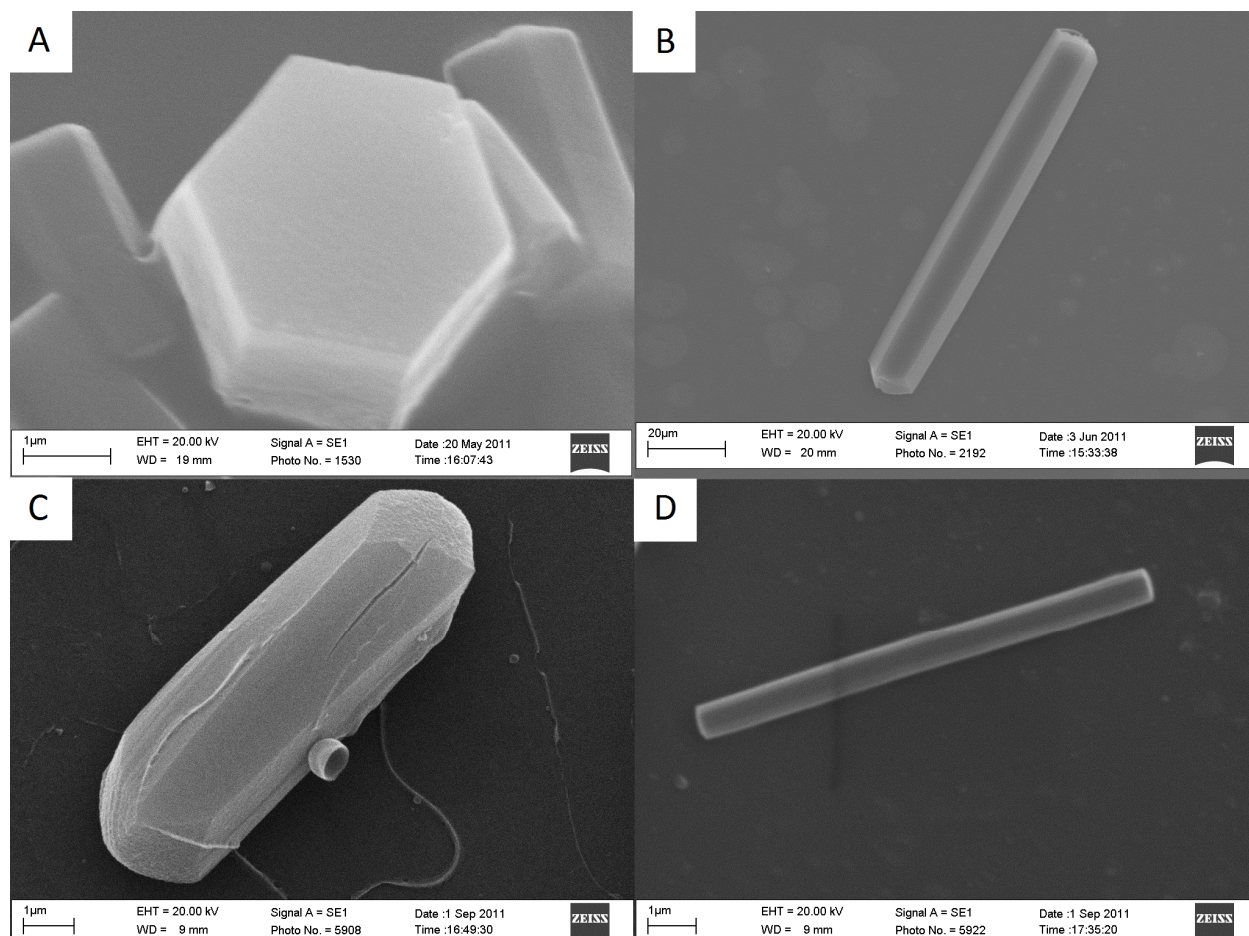


Figure 20: Four Alq₃ samples demonstrating the effect of temperature where a) was made at room temperature with acetone as the anti-solvent, b) was made while refrigerated using acetone as anti-solvent, c) was made at freezer temperatures using THF, and d) was made at freezer temperature using diethyl ether

Znq₂ displayed more fragility in terms of its environmental conditions having to be met to produce a quality crystal. Once again, THF was used to create a supersaturated stock solution which was tested in the three temperature groups, using diethyl ether as the anti-solvent. At room temperature, Znq₂ demonstrates signs of growth proceeding too rapidly, as different crystal lattice orientations were observed in the same polycrystalline group. This is likely due to Znq₂'s molecular structure, which is less planar than Alq₃. It is theorized that this is the primary reason why Znq₂ demonstrates greater sensitivity to environmental conditions when trying to grow single crystals, as it is easier for non-ideal

bonding to take place than it is with Alq_3 . Even on the same sample, multiple distinct morphologies are observed at different locations. See Figure 21. This was never observed with Alq_3 which was consistently hexagonal.

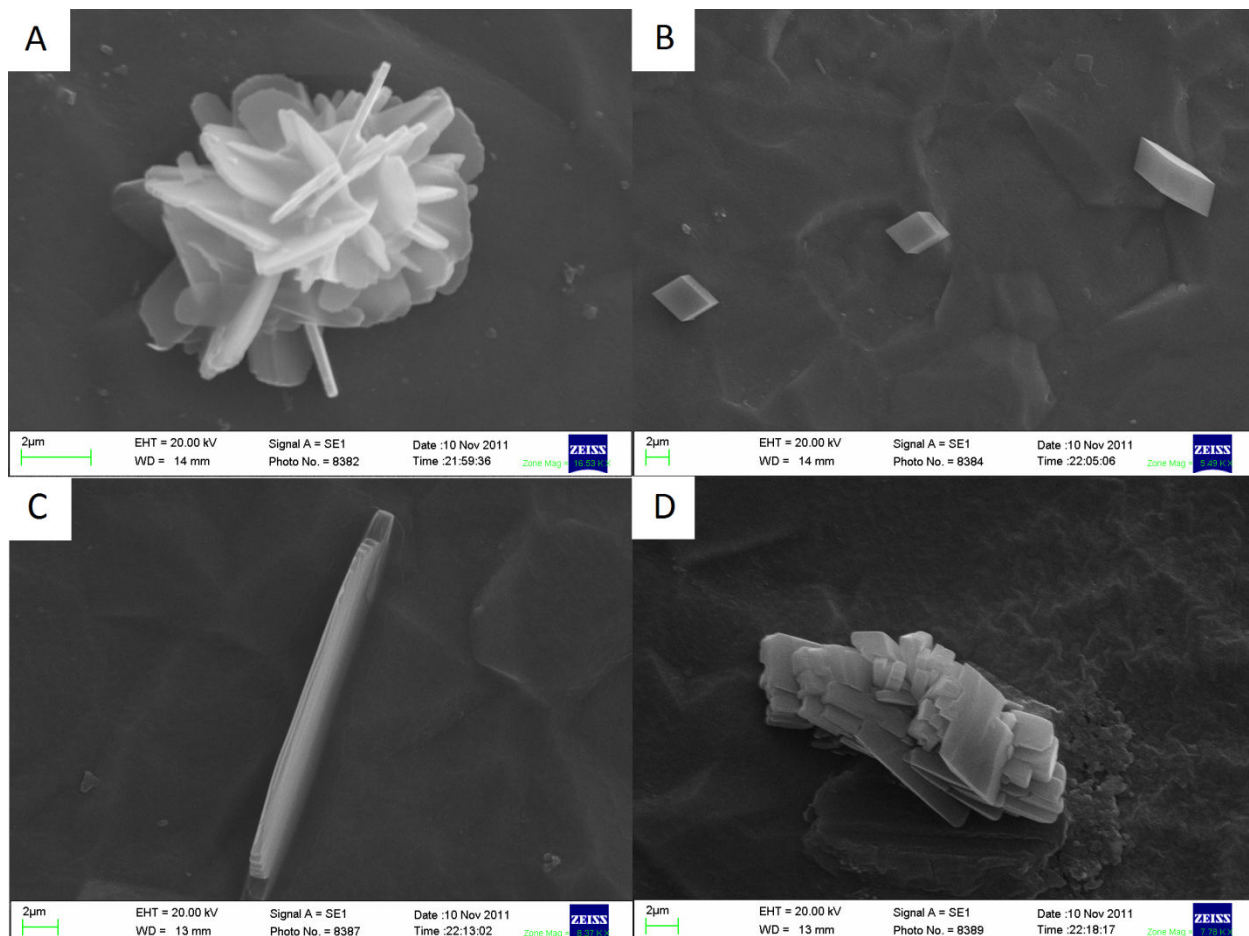


Figure 17: Znq2 samples grown at a-b) refrigerator temperature, c) freezer temperature, d) room temperature

The size of the aperture on top of the sealed container was also an important variable to control, with the ability to influence the quality of crystallization. The initially used parafilm lids were adequate to produce basic results, however the size of the holes were only crudely controllable, as parafilm stretches naturally when pressure is applied to it and because the holes produced via needle were inconsistent in size even when using the same needle. Once the apparatus was upgraded to lids with quantifiably controllable

aperture widths, it became possible to perform more detailed experiments on its effects on the internal pressure of the system.

For Alq₃, it was observed that a high pressure system brought about by a small aperture width had a small but noticeable detrimental effect on the quality of the crystals produced. The hexagonal microrods appeared slightly crushed or twisted. This may be due to the high pressure vapour interfering too much with the liquid stock solution and encouraging non-ideal bonding in the more turbulent molecular environment. The effects of a low pressure system were more noticeable, as the lack of interference with THF's evaporation brought about rapid, chaotic growth in the Alq₃ microrods. See Figure 22.

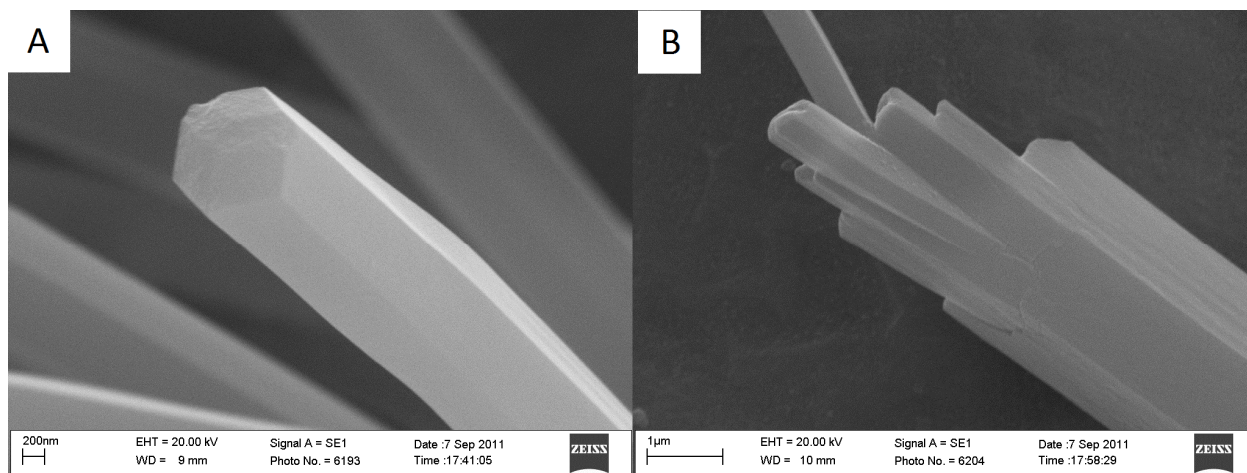


Figure 18: The effects of pressure on Alq₃ crystallization, where a) demonstrates a slight twisting caused by high pressure and b) demonstrates chaotic growth induced by low pressure

In Znq₂, the effects of high and low pressure were similar to those displayed with Alq₃ except that the pressure could also cause fundamental morphological changes. While it is common for multiple different morphologies (half-disks, cubes, dendroids) to be present on a single Znq₂ sample, the ratio of one morphology to the other could be varied via pressure. At high pressure, the cubic morphology (Figure 21b) is more prevalent,

whereas at medium pressure the half-disks are dominant, and at low pressure typically only crude microrods are grown. As with Alq3, the high pressure samples display signs of physical crushing whereas the low pressure samples display poor crystallinity brought about by rapid growth. See Figure 23.

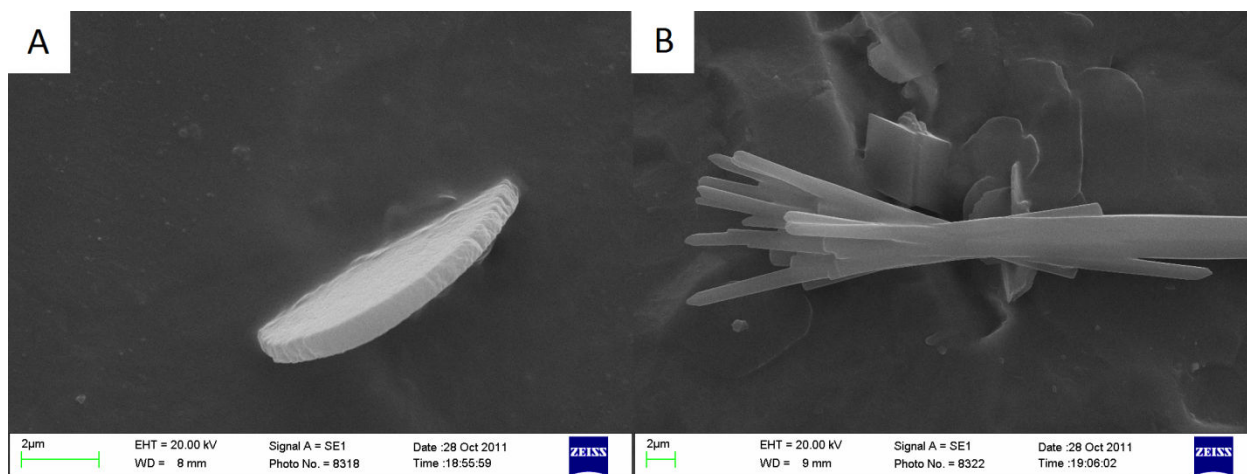


Figure 19: Pressure-induced morphological and crystal quality differences in Znq2. a) was grown under medium pressure, whereas b) was grown under low pressure

Sample exposure time to the anti-solvent vapour is a minor variable, albeit an important one for quality control purposes. If the exposure time was insufficient or overabundant, the quality of the microstructures produced decreased greatly. If the vessel was opened prematurely, then the drop in local pressure greatly accelerated the stock solution evaporation, triggering chaotic structure growth. Conversely, if the vessel remained sealed for an extensive period of time after the stock solution has evaporated, then the ambient anti-solvent eroded the microstructures as a small number of the exposed surface molecules were re-dissolved into the solvent vapour. See Figure 24. Note that the ideal exposure time is the exact time it takes for the stock solution to completely evaporate, with slight overexposure being preferable to underexposure. For an aperture diameter of

0.7mm/0.8mm and an anti-solvent of ether or THF, the ideal time was determined to be 24 hours for both Alq₃ and Znq₂ given a stock solution volume of 20μL.

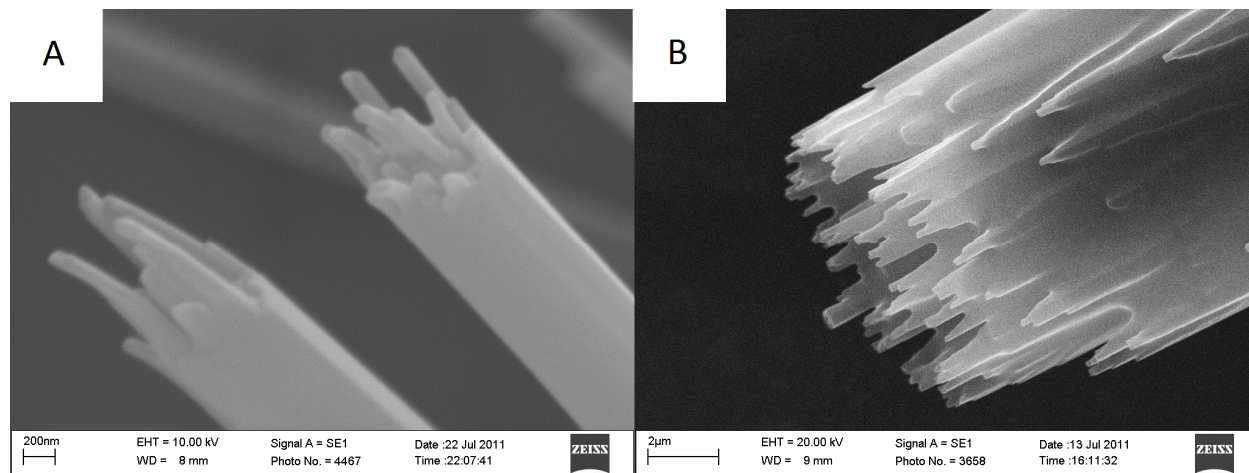


Figure 20: The effects of a) underexposure and b) overexposure to anti-solvent vapours regarding Alq₃ growth

Experimentation was also done using different stock solution solvents beyond THF. CHCl₃ was attempted due to its greater capacity to absorb Alq₃ into solution, but failed to yield any appreciable results when used in a pure form. However, when used in conjunction with THF at a ratio of 87:13 v/v of THF/CHCl₃ (this ideal ratio was determined experimentally), the results were surprisingly useful. Starting with a stock solution supersaturation of 2.8mg/mL in THF/CHCl₃ versus the standard 0.92mg/mL for pure THF, the new stock solution's tripled concentration allowed for a thin film of Alq₃ to form in addition to the standard single crystal microrods. In pure CHCl₃, Alq₃ does not naturally form single crystals however when CHCl₃ only composes a portion of the solvent, it only partially interferes with the crystallization, allowing both an amorphous thin film as well as single crystal rods to form. This results in an array of vertically-oriented single crystal Alq₃ microrods amidst an Alq₃ thin film, as the flat-resting Alq₃ microrods are buried under the thin film blanket. See Figure 25.

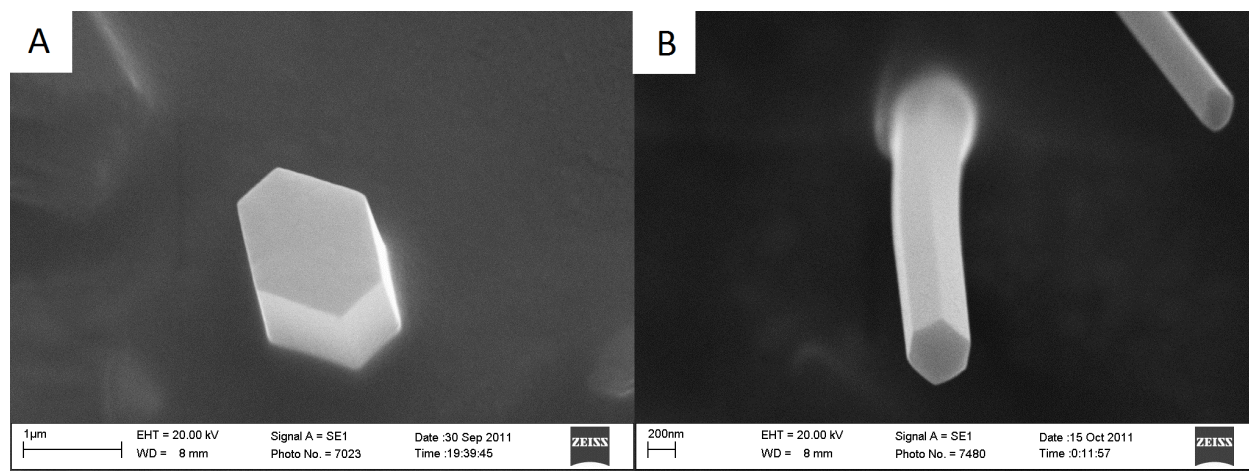


Figure 21: Vertically-oriented single crystal Alq₃ microrods

A second method was also discovered to create an array of vertically-oriented Alq₃ microrods, with a slightly different final result. If a standard supersaturated THF stock solution is deposited on a TiO₂ substrate which has been pre-seeded with an ultrathin 10nm layer of Alq₃ via thermal evaporation, then the Alq₃ in solution will favour growth from the Alq₃ thin film rather than nucleation. The growth will still be of a single crystalline nature. However, the orientation of the crystals will be determined from the thin film where growth begins, meaning that the array of microrods tend to have randomly acute angles from the normal. Because the entirety of the Alq₃ in solution will contribute to the crystalline growth (as opposed to the previous method where most of the Alq₃ went into the thin film), this method produces a much higher density of microrods emanating from the surface, however their orientation tends to be oblique rather than purely vertical. See Figure 26.

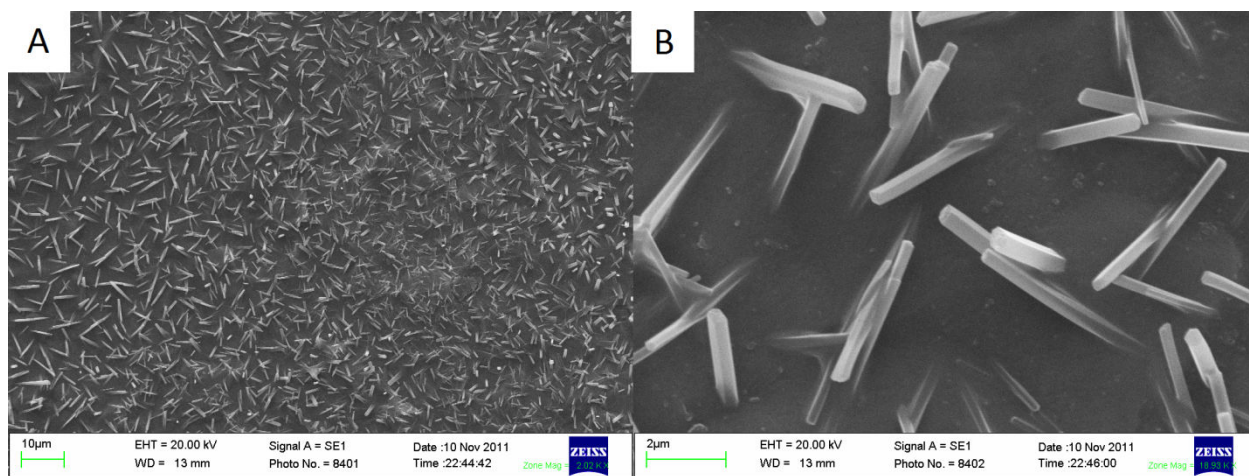


Figure 22: Arrays of Alq₃ microrods formed via pre-seeded growth

Photoluminescence (PL) was also performed on a sample containing a bed of single-crystalline Alq₃ nanorods. With an excitation wavelength fixed at 420nm, the peak photoluminescence was found to be at 515nm. See Figure 27. This visibly differs from the established norm of 530nm[113]. This discrepancy can be accounted for by the varying quality of Alq₃ samples examined. The 530nm baseline figure produced by Garbuzov et. al. was performed on an amorphous thin film produced via thermal evaporation. The peak photoluminescence observed from microrods produced via our self-assembling method is more energetic, suggesting a larger bandgap resulting from tighter inter-molecular spacing. This is also consistent with experimental results in the literature showing that an enhancement in crystallinity increases photoluminescence peak energy as well as a decrease in full-width at half maximum[114]. The narrowing of the peak results from the reduction in defects inside the crystal lattice, which yields more focused PL results and improved charge carrier transport. This evidence supports the clear images showing sharp hexagonal structures indicative of single-crystal Alq₃.

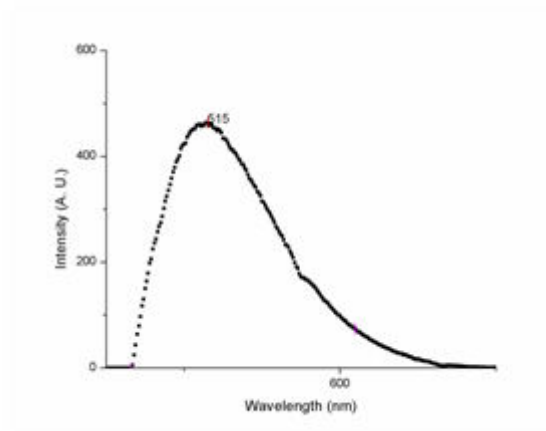


Figure 2723: Photoluminescence performed on Alq3 microrods

Chapter 4: Conclusion

4.1: Conclusion and Future Work

This work explored two distinct areas of nanoscience (organic and inorganic linear nanostructures) though ultimately for the same goal: to gain greater understanding of its properties with the objective of facilitating future device applications.

With regards to organic nanostructures, the semiconductors Alq₃ and Znq₂ were studied with methodical progression so as to examine all the pertinent experimental variables in an evaporation-based solution synthesis. Achieving a high degree of crystallinity as well as expanding morphological control vis-à-vis previous efforts by others using this technique were the priorities for this line of research. To that end, the effects of temperature and ambient vapour pressure (both previously had not been examined in the literature) were recorded and it was found that superior results were obtained when the temperature was near 0°C and when the pressure was regulated above atmospheric levels.

Two novel methods to grow arrays of vertically-oriented crystalline Alq₃ microrods were discovered. The first method relies upon a hybrid stock solution to simultaneously

grow crystalline rods and a thin film. This results in a sparse array of microrods nearly perpendicular to the surface. The second method functions by pre-seeding a thin film of Alq₃ on the surface so as to encourage immediate growth from the thin film instead of the typical nucleation. This results in a dense array of oblique crystalline rods.

Theoretical research was done on dielectrophoresis as a method of attaining individual nanowire samples for study. Afterwards, a DEP testing platform was designed for that purpose. Practical experience was gained in the field of microfabrication in order to build this device, specifically in the fields of thin film deposition and photolithography.

Testing on inorganic semiconducting nanowires have yielded positive results, as the target samples can be reliably aligned despite the inherent hit-or-miss nature of single nanorod alignment. Initial electrical measurements on copper oxide have also yielded reasonable mobility measurements.

There is significant future work to be done in these fields. The methods discovered to grow Alq₃ microrod arrays should be investigated for similar capabilities with regard to Znq₂, the other semiconductors in the quinoline family, as well as pi-conjugated planar organic semiconductors in general. One of the greatest challenges hindering the ascension of organic semiconductors in mainstream technology is the lack of sufficient morphological control for device requirements. A dense array of vertical single-crystal nano and microstructures is a desirable morphology to master for devices which thrive on high-surface area contact layers.

With the DEP alignment and testing device complete and operational, all efforts should be made to align and test as many types of inorganic semiconductors as possible.

The greatest limiting factor is attaining a suitable suspension of nanowires or nanotubes in a liquid with a low dielectric constant and low rate of evaporation. The work in DEP itself has already been largely completed, which concentrates future work in this field into developing suitable nanowire production methods which can accommodate DEP's liquid suspension requirements.

One easily attainable upgrade to the DEP platform would be to partially redesign the photolithography mask such that each pair of electrodes would be segregated onto two new separate masks (with appropriate alignment marks added to each mask) such that each mask would allow for the patterning and deposition of one electrode per pair. By means of this division, two different metals could be used in each diode, allowing for asymmetrical contact pads between the channel. This would unlock a new category of devices which could then be assembled using DEP, as well as augmenting the quantity of scientific data which could be extracted for each semiconductor.

Bibliography

1. Foss Hansen, S., et al., *Late lessons from early warnings for nanotechnology*. Nat Nano, 2008. **3**(8): p. 444-447.
2. Blanco, J., et al., *Limiting Mechanisms of Mode I Interlaminar Toughening of Composites Reinforced with Aligned Carbon Nanotubes*. Journal of Composite Materials, 2009. **43**(8): p. 825-841.
3. Li, X., et al., *Nanoscale Structural and Mechanical Characterization of a Natural Nanocomposite Material: The Shell of Red Abalone*. Nano Letters, 2004. **4**(4): p. 613-617.
4. Abgrall, P., et al., *SU-8 as a structural material for labs-on-chips and microelectromechanical systems*. ELECTROPHORESIS, 2007. **28**(24): p. 4539-4551.
5. Zhang, C.-Y., et al., *Single-quantum-dot-based DNA nanosensor*. Nat Mater, 2005. **4**(11): p. 826-831.
6. Gao, F., et al., *A Novel Nano-Sensor Based on Rhodamine- β -Isothiocyanate – Doped Silica Nanoparticle for pH Measurement*. Microchimica Acta, 2005. **152**(1): p. 131-135.
7. Engel, Y., et al., *Supersensitive Detection of Explosives by Silicon Nanowire Arrays*. Angewandte Chemie International Edition, 2010. **49**(38): p. 6830-6835.
8. Ng, H.T., et al., *Single Crystal Nanowire Vertical Surround-Gate Field-Effect Transistor*. Nano Letters, 2004. **4**(7): p. 1247-1252.
9. Keren, K., et al., *DNA-Templated Carbon Nanotube Field-Effect Transistor*. Science, 2003. **302**(5649): p. 1380-1382.
10. Nguyen, P., et al., *Direct Integration of Metal Oxide Nanowire in Vertical Field-Effect Transistor*. Nano Letters, 2004. **4**(4): p. 651-657.
11. Tennakone, K., et al., *A dye-sensitized nano-porous solid-state photovoltaic cell*. Semiconductor Science and Technology, 1995. **10**(12): p. 1689.
12. Sun, B., E. Marx, and N.C. Greenham, *Photovoltaic Devices Using Blends of Branched CdSe Nanoparticles and Conjugated Polymers*. Nano Letters, 2003. **3**(7): p. 961-963.
13. Wu, Y., et al., *Synthesis and Photovoltaic Application of Copper(I) Sulfide Nanocrystals*. Nano Letters, 2008. **8**(8): p. 2551-2555.
14. <http://www.guardian.co.uk/science/2009/jun/15/carbon-nanotubes-immune-system-nanotechnology> - Retrieved 2012/10/22
15. Tans, S.J., A.R.M. Verschueren, and C. Dekker, *Room-temperature transistor based on a single carbon nanotube*. Nature, 1998. **393**(6680): p. 49-52.
16. Fan, Z., et al., *Three-dimensional nanopillar-array photovoltaics on low-cost and flexible substrates*. Nat Mater, 2009. **8**(8): p. 648-653.
17. Marsillac, S., V.Y. Parikh, and A.D. Compaan, *Ultra-thin bifacial CdTe solar cell*. Solar Energy Materials and Solar Cells, 2007. **91**(15–16): p. 1398-1402.
18. Callister, W.D., *Chapter 3*, in *Fundamentals of Materials Science and Engineering* 2001, John Wiley & Sons Inc. p. 31.
19. Callister, W.D., *Chapter 3*, in *Fundamentals of Materials Science and Engineering* 2001, John Wiley & Sons, Inc. p. 62.
20. *Bravais Lattice*. 2012-12-07]; Available from: http://excellup.com/class_12/chemistry_12/Image_chemistry_12/UnitCell_SevenTypes.GIF.
21. Callister, W.D., *Chapter 5*, in *Fundamentals of Materials Science and Engineering*. 2001, John Wiley & Sons, Inc. p. 103-121.

22. Hu, C.C., *Chapter 1*, in *Modern Semiconductor Devices for Integrated Circuits* 2009, Prentice Hall. p. 5-6.
23. Callister, W.D., *Fundamentals of Materials Science and Engineering*. 5th ed. 2001: John Wiley & Sons, Inc. 103-118.
24. Hu, C.C., *Chapter 5*, in *Modern Semiconductor Devices for Integrated Circuits* 2009, Prentice Hall. p. 173.
25. Hu, C.C., *Chapter 1*, in *Modern Semiconductor Devices for Integrated Circuits* 2009, Prentice Hall. p. 8.
26. Smith, A.M. and S. Nie, *Semiconductor Nanocrystals: Structure, Properties, and Band Gap Engineering*. Accounts of Chemical Research, 2009. **43**(2): p. 190-200.
27. Henry, C.H., *Limiting efficiencies of ideal single and multiple energy gap terrestrial solar cells*. Journal of Applied Physics, 1980. **51**(8): p. 4494-4500.
28. Nakamura, S., et al., *High-Brightness InGaN Blue, Green and Yellow Light-Emitting Diodes with Quantum Well Structures*. Japanese Journal of Applied Physics, 1995. **34**(7A): p. L797.
29. Shockley, W. and H.J. Queisser, *Detailed Balance Limit of Efficiency of p-n Junction Solar Cells*. Journal of Applied Physics, 1961. **32**(3): p. 510-519.
30. Maennig, B., et al., *Controlled p-type doping of polycrystalline and amorphous organic layers: Self-consistent description of conductivity and field-effect mobility by a microscopic percolation model*. Physical Review B, 2001. **64**(19): p. 195208.
31. Gregg, B.A. and R.A. Cormier, *Doping Molecular Semiconductors: n-Type Doping of a Liquid Crystal Perylene Diimide*. Journal of the American Chemical Society, 2001. **123**(32): p. 7959-7960.
32. Gisslen, L., *Influence of Frenkel Excitons and Charge Transfer States on the Spectroscopic Properties of Organic Molecular Crystals*, in *Physics*. 2010, Technical University of Munich: Munich. p. 52.
33. Kazmaier, P.M. and R. Hoffmann, *A Theoretical Study of Crystallochromy. Quantum Interference Effects in the Spectra of Perylene Pigments*. Journal of the American Chemical Society, 1994. **116**(21): p. 9684-9691.
34. Kim, K.S., et al., *Assembling Phenomena of Calix[4]hydroquinone Nanotube Bundles by One-Dimensional Short Hydrogen Bonding and Displaced π - π Stacking*. Journal of the American Chemical Society, 2002. **124**(47): p. 14268-14279.
35. Amundson, K., et al., *12.3: Flexible, Active-Matrix Display Constructed Using a Microencapsulated Electrophoretic Material and an Organic-Semiconductor-Based Backplane*. SID Symposium Digest of Technical Papers, 2001. **32**(1): p. 160-163.
36. Gelinck, G.H., et al., *Flexible active-matrix displays and shift registers based on solution-processed organic transistors*. Nat Mater, 2004. **3**(2): p. 106-110.
37. Huitema, H.E.A., et al., *Plastic transistors in active-matrix displays*. Nature, 2001. **414**(6864): p. 599-599.
38. Someya, T., et al., *Conformable, flexible, large-area networks of pressure and thermal sensors with organic transistor active matrixes*. Proceedings of the National Academy of Sciences of the United States of America, 2005. **102**(35): p. 12321-12325.
39. Sekitani, T., et al., *Organic Nonvolatile Memory Transistors for Flexible Sensor Arrays*. Science, 2009. **326**(5959): p. 1516-1519.
40. MANUNZA, et al., *Pressure sensing by flexible, organic, field effect transistors*. Vol. 89. 2006, Melville, NY, ETATS-UNIS: American Institute of Physics.

41. Zschieschang, U., et al., *Flexible Low-Voltage Organic Transistors and Circuits Based on a High-Mobility Organic Semiconductor with Good Air Stability*. *Advanced Materials*, 2010. **22**(9): p. 982-985.
42. BONFIGLIO, et al., *A completely flexible organic transistor obtained by a one-mask photolithographic process*. Vol. 82. 2003, Melville, NY, ETATS-UNIS: American Institute of Physics. 3.
43. Bradley, K., J.-C.P. Gabriel, and G. Grüner, *Flexible Nanotube Electronics*. *Nano Letters*, 2003. **3**(10): p. 1353-1355.
44. *OLED*. 2012-11-15]; Available from: http://3.bp.blogspot.com/-PHLXkaNrmZ4/T8TLfeLHDil/AAAAAAAAAig/CPFmsGaK_i8/s640/OLED_EarlyProduct.JPG.
45. Wagner, R.S. and W.C. Ellis, *VAPOR-LIQUID-SOLID MECHANISM OF SINGLE CRYSTAL GROWTH*. *Applied Physics Letters*, 1964. **4**(5): p. 89-90.
46. Xue, F., et al., *Solvothermal synthesis and photoluminescence properties of BiPO₄ nano-cocoons and nanorods with different phases*. *Journal of Solid State Chemistry*, 2009. **182**(6): p. 1396-1400.
47. Martin, C.R., *Membrane-Based Synthesis of Nanomaterials*. *Chemistry of Materials*, 1996. **8**(8): p. 1739-1746.
48. Jiang, L., et al., *Single-Crystalline, Size, and Orientation Controllable Nanowires and Ultralong Microwires of Organic Semiconductor with Strong Photoswitching Property*. *Journal of the American Chemical Society*, 2008. **130**(12): p. 3937-3941.
49. Kloc, C., et al., *Physical vapor growth of centimeter-sized crystals of α -hexathiophene*. *Journal of Crystal Growth*, 1997. **182**(3-4): p. 416-427.
50. Chen, W., Q. Peng, and Y. Li, *Alq₃ Nanorods: Promising Building Blocks for Optical Devices*. *Advanced Materials*, 2008. **20**(14): p. 2747-2750.
51. Kashchiev, D., *Preface*, in *Nucleation*. 2000, Butterworth-Heinemann: Oxford. p. ix-xii.
52. Mullin, J.W., *Crystallization*. Chemical, Petrochemical & Process. 2001: Elsevier Butterworth-Heinemann. 1-600.
53. Cubillas, P. and M.W. Anderson, *Synthesis Mechanism: Crystal Growth and Nucleation*, in *Zeolites and Catalysis*. 2010, Wiley-VCH Verlag GmbH & Co. KGaA. p. 1-55.
54. *Gibbs Free Energy graph*. 2012-11-10 2012-11-10; Available from: http://homes.esat.kuleuven.be/~igemwiki/images/thermodynamics/thermo_fig2.jpg.
55. Kashchiev, D. and G.M. van Rosmalen, *Review: Nucleation in solutions revisited*. *Crystal Research and Technology*, 2003. **38**(7-8): p. 555-574.
56. Pohl, H.A., *Dielectrophoresis*. 1978, Cambridge: Cambridge University Press.
57. Pethig, R., *Review article-dielectrophoresis: status of the theory, technology, and applications*. *Biomicrofluidics*, 2010. **4**(2).
58. *DEP figure*, retrieved 2012-10-25. Available from: http://matthieu.lagouge.free.fr/elecstq/elecstq_pict/dep_demo.png.
59. Seo, H.-W., et al., *Controlled assembly of single SWNTs bundle using dielectrophoresis*. *Microelectronic Engineering*, 2005. **81**(1): p. 83-89.
60. Lutz, T. and K.J. Donovan, *Macroscopic scale separation of metallic and semiconducting nanotubes by dielectrophoresis*. *Carbon*, 2005. **43**(12): p. 2508-2513.
61. Kim, S., et al., *Single-walled carbon nanotube transistors fabricated by advanced alignment techniques utilizing CVD growth and dielectrophoresis*. *Solid-State Electronics*, 2008. **52**(8): p. 1260-1263.
62. Li, J., et al., *Fabrication of carbon nanotube field effect transistors by AC dielectrophoresis method*. *Carbon*, 2004. **42**(11): p. 2263-2267.

63. Nocke, A., et al., *Polymer composite strain sensor based on dielectrophoretically aligned tellurium nanorods*. *Procedia Chemistry*, 2009. **1**(1): p. 1151-1154.
64. Liu, W.J., et al., *Dielectrophoretic manipulation of nano-materials and its application to micro/nano-sensors*. *Sensors and Actuators B: Chemical*, 2008. **133**(2): p. 664-670.
65. Lucci, M., et al., *Gas sensing using single wall carbon nanotubes ordered with dielectrophoresis*. *Sensors and Actuators B: Chemical*, 2005. **111–112**(0): p. 181-186.
66. Suehiro, J., et al., *Controlled fabrication of carbon nanotube NO₂ gas sensor using dielectrophoretic impedance measurement*. *Sensors and Actuators B: Chemical*, 2005. **108**(1–2): p. 398-403.
67. Suehiro, J., et al., *Schottky-type response of carbon nanotube NO₂ gas sensor fabricated onto aluminum electrodes by dielectrophoresis*. *Sensors and Actuators B: Chemical*, 2006. **114**(2): p. 943-949.
68. Mahmoodi, S.R., et al., *Dielectrophoretic assembly of ZnO nanorods for gas sensing*. *Procedia Chemistry*, 2009. **1**(1): p. 947-950.
69. Suehiro, J., et al., *Fabrication of interfaces between carbon nanotubes and catalytic palladium using dielectrophoresis and its application to hydrogen gas sensor*. *Sensors and Actuators B: Chemical*, 2007. **127**(2): p. 505-511.
70. Lee, S.Y., et al., *A study of dielectrophoretically aligned gallium nitride nanowires in metal electrodes and their electrical properties*. *Chemical Physics Letters*, 2006. **427**(1–3): p. 107-112.
71. Lee, S.Y., et al., *An electrical characterization of a hetero-junction nanowire (NW) PN diode (n-GaN NW/p-Si) formed by dielectrophoresis alignment*. *Physica E: Low-dimensional Systems and Nanostructures*, 2007. **36**(2): p. 194-198.
72. Lee, J.-W., et al., *Dielectrophoretic assembly of GaN nanowires for UV sensor applications*. *Solid State Communications*, 2008. **148**(5–6): p. 194-198.
73. Lee, S.-Y., et al., *The synthesis of ZnO nanowires and their subsequent use in high-current field-effect transistors formed by dielectrophoresis alignment*. *Physica E: Low-dimensional Systems and Nanostructures*, 2008. **40**(4): p. 866-872.
74. Seo, Y.-K., S. Kumar, and G.-H. Kim, *Photoconductivity characteristics of ZnO nanoparticles assembled in nanogap electrodes for portable photodetector applications*. *Physica E: Low-dimensional Systems and Nanostructures*, 2010. **42**(4): p. 1163-1166.
75. Lee, H.J., et al., *Simple and rapid preparation of vertically aligned gold nanoparticle arrays and fused nanorods in pores of alumina membrane based on positive dielectrophoresis*. *Sensors and Actuators B: Chemical*, 2009. **136**(2): p. 320-325.
76. Lumsdon, S.O., E.W. Kaler, and O.D. Velez, *Two-Dimensional Crystallization of Microspheres by a Coplanar AC Electric Field*. *Langmuir*, 2004. **20**(6): p. 2108-2116.
77. Becker, F.F., et al., *The removal of human leukaemia cells from blood using interdigitated microelectrodes*. *Journal of Physics D: Applied Physics*, 1994. **27**(12): p. 2659.
78. Gascoyne, P., et al., *Dielectrophoretic detection of changes in erythrocyte membranes following malarial infection*. *Biochimica et Biophysica Acta (BBA) - Biomembranes*, 1997. **1323**(2): p. 240-252.
79. Nascimento, E.M., et al., *Dielectrophoretic sorting on a microfabricated flow cytometer: Label free separation of Babesia bovis infected erythrocytes*. *Bioelectrochemistry*, 2008. **73**(2): p. 123-128.
80. Hashimoto, M., H. Kaji, and M. Nishizawa, *Selective capture of a specific cell type from mixed leucocytes in an electrode-integrated microfluidic device*. *Biosensors and Bioelectronics*, 2009. **24**(9): p. 2892-2897.
81. Müller, T., et al., *High frequency electric fields for trapping of viruses*. *Biotechnology Techniques*, 1996. **10**(4): p. 221-226.

82. Morgan, H. and N.G. Green, *Dielectrophoretic manipulation of rod-shaped viral particles*. Journal of Electrostatics, 1997. **42**(3): p. 279-293.
83. Akin, D., H. Li, and R. Bashir, *Real-Time Virus Trapping and Fluorescent Imaging in Microfluidic Devices*. Nano Letters, 2003. **4**(2): p. 257-259.
84. Palik, E.D., *Handbook of Optical Constants of Solids*, Elsevier.
85. Allam, N.K. and C.A. Grimes, *Electrochemical fabrication of complex copper oxide nanoarchitectures via copper anodization in aqueous and non-aqueous electrolytes*. Materials Letters, 2011. **65**(12): p. 1949-1955.
86. Wu, X., et al., *Copper Hydroxide Nanoneedle and Nanotube Arrays Fabricated by Anodization of Copper*. The Journal of Physical Chemistry B, 2005. **109**(48): p. 22836-22842.
87. Zhang, W., et al., *Single-Crystalline Scroll-Type Nanotube Arrays of Copper Hydroxide Synthesized at Room Temperature*. Advanced Materials, 2003. **15**(10): p. 822-825.
88. Park, S.-H. and H.J. Kim, *Unidirectionally Aligned Copper Hydroxide Crystalline Nanorods from Two-Dimensional Copper Hydroxy Nitrate*. Journal of the American Chemical Society, 2004. **126**(44): p. 14368-14369.
89. Du, G.H. and G. Van Tendeloo, *Cu(OH)₂ nanowires, CuO nanowires and CuO nanobelts*. Chemical Physics Letters, 2004. **393**(1-3): p. 64-69.
90. Lu, C., et al., *Simple Template-Free Solution Route for the Controlled Synthesis of Cu(OH)₂ and CuO Nanostructures*. The Journal of Physical Chemistry B, 2004. **108**(46): p. 17825-17831.
91. Zhang, W., et al., *Growth of novel nanostructured copper oxide (CuO) films on copper foil*. Journal of Crystal Growth, 2006. **291**(2): p. 479-484.
92. Wen, X., W. Zhang, and S. Yang, *Synthesis of Cu(OH)₂ and CuO Nanoribbon Arrays on a Copper Surface*. Langmuir, 2003. **19**(14): p. 5898-5903.
93. Briseno, A.L., et al., *Patterned Growth of Large Oriented Organic Semiconductor Single Crystals on Self-Assembled Monolayer Templates*. Journal of the American Chemical Society, 2005. **127**(35): p. 12164-12165.
94. Gelinck, G.H., T.C.T. Geuns, and D.M. de Leeuw, *High-performance all-polymer integrated circuits*. Applied Physics Letters, 2000. **77**(10): p. 1487-1489.
95. Sirringhaus, H., N. Tessler, and R.H. Friend, *Integrated Optoelectronic Devices Based on Conjugated Polymers*. Science, 1998. **280**(5370): p. 1741-1744.
96. Moon, H., et al., *Synthesis, Crystal Structure, and Transistor Performance of Tetracene Derivatives*. Journal of the American Chemical Society, 2004. **126**(47): p. 15322-15323.
97. Hu, J.-S., et al., *Facile solution synthesis of hexagonal Alq₃ nanorods and their field emission properties*. Chemical Communications, 2007(29): p. 3083-3085.
98. Lo, S.-S., et al., *A single Alq₃ submicro-wire Schottky diode and its negative differential resistance*. Journal of Materials Chemistry, 2012. **22**(25): p. 12618-12621.
99. Xu, G., et al., *Facile solution synthesis without surfactant assistant for ultra long Alq₃ sub-microwires and their enhanced field emission and waveguide properties*. Journal of Materials Chemistry, 2010. **20**(15): p. 3006-3010.
100. Whitesides, G.M. and B. Grzybowski, *Self-Assembly at All Scales*. Science, 2002. **295**(5564): p. 2418-2421.
101. Tung, H.-H., J.A. McCauley, and M. Midler, *Crystallization of Organic Compounds : An Industrial Perspective*. 2009, Hoboken, NJ, USA: Wiley.
102. Kang, J.H. and X.Y. Zhu, *Pi-stacked pentacene thin films grown on Au(111)*. Applied Physics Letters, 2003. **82**(19): p. 3248.
103. Lim, J.A., et al., *Control of the Morphology and Structural Development of Solution-Processed Functionalized Acenes for High-Performance Organic Transistors*. Advanced Functional Materials, 2009. **19**(10): p. 1515-1525.

104. Minemawari, H., et al., *Inkjet printing of single-crystal films*. Nature, 2011. **475**(7356): p. 364-367.
105. Smith, P.A., et al., *Electric-field assisted assembly and alignment of metallic nanowires*. Applied Physics Letters, 2000. **77**(9).
106. Dong, L., et al., *Dielectrophoretically Controlled Fabrication of Single-Crystal Nickel Silicide Nanowire Interconnects*. Nano Letters, 2005. **5**(10): p. 2112-2115.
107. Ngoi, G.U.a.B.K.A., *Surface Topography Analysis of Silicon Wafers by a Chromameter*. American Society for Precision Engineering, 2000. **2000 Annual Proceedings**.
108. Franssila, S., *Introduction to Microfabrication*. 2010.
109. Han, J.-W. and M. Meyyappan, *Copper oxide resistive switching memory for e-textile*. AIP Advances, 2011. **1**(3): p. 032162-8.
110. Dong, R., et al., *Reproducible hysteresis and resistive switching in metal-Cu_xO-metal heterostructures*. Applied Physics Letters, 2007. **90**(4): p. 042107-3.
111. Chen, A., et al., *Switching characteristics of Cu₂O metal-insulator-metal resistive memory*. Applied Physics Letters, 2007. **91**(12): p. 123517-3.
112. Wypych, G., *Knovel Solvents - A Properties Database*, ChemTec Publishing.
113. Garbuzov, D.Z., et al., *Photoluminescence efficiency and absorption of aluminum-tris-quinolate (Alq₃) thin films*. Chemical Physics Letters, 1996. **249**(5–6): p. 433-437.
114. Kim, K.-K., et al., *The grain size effects on the photoluminescence of ZnO/alpha-Al₂O₃ grown by radio-frequency magnetron sputtering*. Journal of Applied Physics, 2000. **87**(7): p. 3573-3575.